JAMES | Journal of Advances in Modeling Earth Systems

RESEARCH ARTICLE
10.1029/2021MS002562

Key Points:

- A new coupled atmospheric-hydrological regional modeling system of water isotopologues is presented
- Land surface evaporation fractionation increases the isotopic concentrations in the rootzone
- Lateral terrestrial water flow has a minor effect on isotopic concentrations in the rootzone

Correspondence to:
J. Arnault,
joel.arnault@kit.edu

Citation:
Arnault, J., Jung, G., Haese, B., Fersch, B., Rummler, T., Wei, J., et al. (2021). A joint soil-vegetation-atmospheric modeling procedure of water isotopologues: Implementation and application to different climate zones with WRF-Hydro-iso. *Journal of Advances in Modeling Earth Systems*, *13*, e2021MS002562. https://doi.org/10.1029/2021MS002562

Received 8 APR 2021
Accepted 16 SEP 2021

A Joint Soil-Vegetation-Atmospheric Modeling Procedure of Water Isotopologues: Implementation and Application to Different Climate Zones With WRF-Hydro-Iso

Joël Arnault[1], Gerlinde Jung[2], Barbara Haese[3], Benjamin Fersch[1], Thomas Rummler[3], Jianhui Wei[1], Zhenyu Zhang[1,3], and Harald Kunstmann[1,3]

[1]Institute of Meteorology and Climate Research, Karlsruhe Institute of Technology, Garmisch-Partenkirchen, Germany, [2]Bremen, Germany, [3]Institute of Geography, University of Augsburg, Augsburg, Germany

Abstract Water isotopologues, as natural tracers of the hydrological cycle on Earth, provide a unique way to assess the skill of climate models in representing realistic atmospheric-terrestrial water pathways. This study presents the newly developed WRF-Hydro-iso, which is a version of the coupled atmospheric-hydrological WRF-Hydro model enhanced with a joint soil-vegetation-atmospheric description of water isotopologue motions. It allows the consideration of isotopic fractionation processes during water phase changes in the atmosphere, the land surface, and the subsurface. For validation, WRF-Hydro-iso is applied to two different climate zones, namely Europe and Southern Africa under the present climate conditions. Each case is modeled with a domain employing a 5 km grid-spacing coupled with a terrestrial subgrid employing a 500 m grid-spacing in order to represent lateral terrestrial water flow. A 10-year slice is simulated for 2003–2012, using ERA5 reanalyses as driving data. The boundary condition of isotopic variables is prescribed with mean values from a 10-year simulation with the Community Earth System Model Version 1. WRF-Hydro-iso realistically reproduces the climatological variations of the isotopic concentrations $\delta_P{}^{18}$O and $\delta_P{}^{2}$H from the Global Network of Isotopes in Precipitation. In a sensitivity analysis, it is found that land surface evaporation fractionation increases the isotopic concentrations in the rootzone soil moisture and slightly decreases the isotopic concentrations in precipitation. Lateral terrestrial water flow minorly affects these isotopic concentrations through changes in evaporation-transpiration partitioning.

Plain Language Summary Global climate models are limited by their coarse resolution, which may reduce their meaningfulness. This problem can be circumvented for a specific region with regional climate models, which provide, for example, a detailed description of clouds and land-atmosphere interactions. But it remains a question: How realistic is the model representation of water transport through the different compartments of the hydrological cycle, the atmosphere, the land, and the sea? A unique way to assess modeled water transport is the comparison to natural tracers, such as water isotopologues, which requires to include the fate of these water isotopologues in the model. This is what we pursue here with the newly developed WRF-Hydro-iso model. A model description and a proof of concept are provided for two climate zones, using the Global Network of Isotopes in Precipitation data set as reference.

1. Introduction

Water isotopologues, namely water molecules that contain an isotope of oxygen or hydrogen, are natural tracers that characterize the Earth's water cycle in the present and past days (Gat, 1996), which is the reason why their observation and modeling has been raising the interest of the scientific community for many decades (e.g., Dansgaard, 1954; Joussaume et al., 1984; Steen-Larsen et al., 2017). In this work, the focus is on modeling the isotopic fractionation processes in the coupled land-atmosphere regional water cycle. This is developed and achieved with the coupled atmospheric-hydrological regional modeling system WRF-Hydro (Gochis et al., 2018). The objective is to evaluate the benefit of using WRF-Hydro for representing water isotopologues.

The most abundant water molecule on Earth is $^{1}H_2{}^{16}O$, with an average abundance of 99.77%. The remaining water molecules mainly consist of the stable isotopologues $^{1}H_2{}^{18}O$ and $^{1}H{}^{2}H{}^{16}O$, with respective

average abundances of 0.20% and 0.03% (Dansgaard, 1964). Local departures from these average abundances are related to temperature-dependent isotopic fractionation processes occurring during water phase changes involving the gaseous phase (Majoube, 1971a, 1971b; Merlivat & Nief, 1967), the depletion of $^{1}H_{2}{}^{18}O$ and $^{1}H\,{}^{2}H{}^{16}O$ in the gaseous phase being enhanced with decreasing temperature. Such isotopic variations are usually evaluated as δ-values of isotopic concentration ratios $\delta^{18}O$ and $\delta^{2}H$:

$$\delta^{18}O = \left(\frac{\frac{\left[{}^{1}H_{2}{}^{18}O\right]}{\left[{}^{1}H_{2}{}^{16}O\right]}}{\frac{\left[{}^{1}H_{2}{}^{18}O\right]_{VSMOW}}{\left[{}^{1}H_{2}{}^{16}O\right]_{VSMOW}}} - 1 \right) \times 1{,}000 \quad (1)$$

and

$$\delta^{2}H = \left(\frac{\frac{\left[{}^{1}H\,{}^{2}H{}^{16}O\right]}{\left[{}^{1}H_{2}{}^{16}O\right]}}{\frac{\left[{}^{1}H\,{}^{2}H{}^{16}O\right]_{VSMOW}}{\left[{}^{1}H_{2}{}^{16}O\right]_{VSMOW}}} - 1 \right) \times 1{,}000 \quad (2)$$

where the brackets indicate a concentration and subscript VSMOW stands for the Vienna Standard Mean Ocean Water. The δ-values of isotopic concentration ratios for precipitation, namely $\delta_P{}^{18}O$ and $\delta_P{}^{2}H$, have been measured worldwide since 1961 within the Global Network of Isotopes in Precipitation (GNIP) of the International Atomic Energy Agency and the World Meteorology Organization (IAEA/WMO, 2020). $\delta_P{}^{18}O$ and $\delta_P{}^{2}H$ mostly decrease with the temperature, leading to the so-called "latitude effect" and "altitude effect," but also with the distance to the coast, leading to the so-called "continental effect" (e.g., Dansgaard, 1964). In tropical regions, the "temperature effect" is replaced by a weaker relation between precipitation isotopic concentrations and the amount of precipitation, the so-called "amount effect" (e.g., Dansgaard, 1964).

The dependency of $\delta^{18}O$ and $\delta^{2}H$ to temperature provides a unique way to evaluate past climate conditions using paleo records (e.g., Dansgaard et al., 1969). However, the accuracy of the climatic interpretation of paleo records can be hampered by a lack of knowledge of the processes affecting water isotopologues through the Earth's water cycle, such as during sub-cloud rain droplet evaporation (e.g., Friedman et al., 1962) and land surface evaporation (e.g., Jacob & Sonntag, 1991).

Global models have been enhanced with the description of $\delta^{18}O$ and $\delta^{2}H$ to test their ability in reproducing isotopic climatic signals from the past and present days (e.g., Eckstein et al., 2018; Haese et al., 2013; Hoffmann et al., 1998; Joussaume et al., 1984; Nusbaumer et al., 2017; Risi, et al., 2010, 2016; Werner et al., 2016; Wong et al., 2017), and also to identify systematic model biases (e.g., Risi et al., 2012). Global models are limited by their relatively coarse resolutions and crude representation of clouds, which largely impact the simulation of isotopic concentrations (e.g., Nusbaumer et al., 2017). A more accurate matching between modeled and observed $\delta^{18}O$ and $\delta^{2}H$ can be reached with a finer resolution of cloud processes using regional models, as shown, for example, by Moore et al. (2016) with the Weather Research and Forecasting model (WRF, Skamarock & Klemp, 2008) and by Pfahl et al. (2012) and Aemisegger et al. (2015) with the Consortium for Small-scale Modeling (COSMO, Steppeler et al., 2003). In a sensitivity analysis with COSMO$_{iso}$ (Pfahl et al., 2012) for Europe, Christner et al. (2018) showed that $\delta_P{}^{2}H$ during summer is mainly related to the degree of rainout of air masses, with a smaller influence from rain droplet evaporation and land surface evaporation.

Recent developments in regional modeling have confirmed that coupling a sophisticated terrestrial hydrology model with an atmospheric model modifies the simulated hydrological cycle (e.g., Anyah et al., 2008; Larsen et al., 2016; Maxwell et al., 2011; Sulis et al., 2018; Wagner et al., 2016). Using the hydrologically enhanced WRF model referred to as WRF-Hydro (Gochis et al., 2018), it has been shown that the consideration of overland and subsurface water flow generally increases the soil water storage, land surface evaporation, and precipitation (e.g., Arnault et al., 2021, 2018; Arnault, Knoche, et al., 2016; Arnault, Wagner,

et al., 2016; Fersch et al., 2020; Rummler et al., 2019; Zhang et al., 2019). The question arises whether lateral terrestrial water flow also affects the concentration of water isotopologues through the Earth's water cycle. This is especially relevant for the interpretation of paleo records, which have potentially been altered by soil water transport (e.g., Konecky et al., 2020).

WRF-Hydro has recently been enhanced with a joint soil-vegetation-atmospheric water tagging procedure (WRF-Hydro-tag, Arnault et al., 2019), which allows to trace precipitation water from a source region through the land water compartments and in the atmosphere for the evaporated part. Enhancing WRF-Hydro-tag with isotopic fractionation processes during water phase changes allows now to also describe the fate of water isotopologues in the simulated land-atmosphere system.

This study presents the newly developed WRF-Hydro-iso modeling system, that is, a version of WRF-Hydro-tag adapted to the description of water isotopologues. The aim is to assess the effect of lateral terrestrial water flow on modeled isotopic concentrations and evaluate the potential of WRF-Hydro-iso to improve the interpretation of paleo records. For the case-study application, we choose to simulate and compare two present-day climate cases: the first one for Europe where many GNIP station observations are available (IAEA/WMO, 2020) and the second one for Southern Africa. The second application case is chosen in order to further investigate the potential alteration of Southern African paleo records data by soil processes (e.g., Herrmann et al., 2017), and better understand past- and present-day climate variations in Southern Africa (e.g., Weldeab et al., 2013) with the help of water isotopologue modeling. Section 2 of the paper describes the implementation of WRF-Hydro-iso. The application case studies are presented in Section 3, and the climate and water isotopologue modeling results are detailed in Sections 4 and 5. A summary and perspectives are finally given in Section 6.

2. Water Isotopologue Modeling Procedure

2.1. About WRF-Hydro-Tag

WRF-Hydro-tag is a version of the coupled atmospheric-hydrological model WRF-Hydro from Gochis et al. (2018), which has been enhanced with a tagged water cycle (Arnault et al., 2019). This tagged water cycle is initialized to zero and a source of tagged water is defined for a given area and a given time period. During the model run, the fate of this water source is tracked using the tagged water cycle through the modeled water compartments that are the atmosphere, snow cover, vegetation canopy, and soil.

As in Arnault et al. (2021), the version of WRF-Hydro-tag considered in this study is based on the WRF version 4.0 and the hydrological module of WRF-Hydro version 5.0, and the selected physics parameterization options are the six-class WSM6 microphysics scheme of Hong and Lim (2006), the ACM2 atmospheric turbulence scheme of Pleim (2007), and the Noah-MP community Noah land surface model (LSM) with multi-parameterization options of Niu et al. (2011). WRF-Hydro-tag can be run with subsurface, overland, and channel flow routing, as well as a bucket model to estimate baseflow (Gochis et al., 2018). If no routing option is activated, the infiltration excess from Noah-MP represents the surface runoff. If a routing option is activated, the infiltration excess becomes a source of surface ponded water, and the routing of surface ponded water and liquid soil moisture is calculated on a subgrid coupled with the LSM. In this case, surface runoff happens when the surface ponded water reaches a river grid cell. The channel routing and bucket model are used to estimate river streamflow, although the water, which has entered a river does not interact with the LSM in this model version. In the following, channel routing and bucket model are not considered, and the focus is on the spatial redistribution of terrestrial water through overland and subsurface flow.

With this configuration, the water variables, which are duplicated for the description of the tagged water cycle are, (a) for the atmospheric part: the mixing ratios of water vapor, cloud water, cloud ice, rain water, snow, and graupel, and (b) for the terrestrial part: the snowpack equivalent water heights as solid and liquid phases, liquid and frozen canopy water heights, surface ponded water height, and liquid and frozen soil moisture volumetric ratios in a four-layer soil column of 2 m depth. The fate of the tagged water variables is resolved with additionally implemented tagged prognostic equations, as detailed by Arnault, Knoche, et al. (2016) and Arnault, Wagner, et al. (2016) for the atmospheric part, and by Arnault et al. (2019) for the terrestrial part.

2.2. Adaptation of WRF-Hydro-Tag to WRF-Hydro-Iso

WRF-Hydro-iso is developed from WRF-Hydro-tag, by considering that the tagged water cycle represents the cycle of a water isotopologue. Following previous water isotopologue modeling developments (e.g., Nusbaumer et al., 2017; Pfahl et al., 2012), the original water variables in the model are assumed to represent the fate of the most abundant water molecule $^{1}H_2\,^{16}O$. Two additional tagged water cycles are implemented in WRF-Hydro-iso, the first one for $^{1}H_2\,^{18}O$ using tagged water variables labeled as iso1 variables, and the second one for $^{1}H\,^{2}H\,^{16}O$ using tagged water variable labeled as iso2 variables.

A technical difference between WRF-Hydro-tag and WRF-Hydro-iso is that there is no source of traced water to be defined for a specific area and period in WRF-Hydro-iso, but instead, the initial and lateral boundary conditions of the isotopic water variables need to be prescribed from additional data source. Moreover, the iso1 variables implemented in WRF-Hydro-iso are normalized by the VSMOW concentration ratio $\left[{}^{1}H_2\,{}^{18}O\right]_{VSMOW}/\left[{}^{1}H_2\,{}^{16}O\right]_{VSMOW}$, and the iso2 variables by the ratio $\left[{}^{1}H\,{}^{2}H\,{}^{16}O\right]_{VSMOW}/\left[{}^{1}H_2\,{}^{16}O\right]_{VSMOW}$. Accordingly, the δ-values of isotopic concentration ratios (1) and (2) can be post processed from WRF-Hydro-iso outputs as:

$$\delta_M\,{}^{18}O = \left(\frac{M^{iso1}}{M} - 1\right) \times 1{,}000 \tag{3}$$

and

$$\delta_M\,{}^{2}H = \left(\frac{M^{iso2}}{M} - 1\right) \times 1{,}000 \tag{4}$$

where M stands for a water variable, and M^{iso} stands for the corresponding isotopic variable. In the following, $\delta_M\,{}^{18}O$ and $\delta_M\,{}^{2}H$ are referred to as δ_M^{iso}.

2.3. Isotopic Fractionation Processes in WRF-Hydro-Iso

A realistic description of the fate of water isotopologues in WRF-Hydro-iso necessitates the consideration of isotopic fractionation processes during water phase changes involving the gaseous phase (Majoube, 1971a, 1971b; Merlivat & Nief, 1967). Water isotopologue models usually include the isotopic fractionation occurring during sea surface evaporation and cloud formation, as originally documented by Merlivat and Jouzel (1979). A distinction between isotopic equilibrium fractionation occurring during the condensation of cloud droplets and instantaneous extraction fractionation during the generation of ice nuclei, is generally accounted for (e.g., Blossey et al., 2010; Hoffmann et al., 1998; Nusbaumer et al., 2017; Pfahl et al., 2012). The consideration of the isotopic fractionation occurring during rain droplet evaporation is also important to better match observed isotopic concentrations, as shown, for example, by Christner et al. (2018), Field et al. (2010), and Risi et al. (2008). Isotopic fractionation occurring during land surface evaporation recently raised particular interest (e.g., Christner et al., 2018; Haese et al., 2013), as this may affect precipitation isotopic concentrations in regions characterized by large moisture recycling (Aemisegger et al., 2014).

The following subsections detail how these isotopic fractionation processes are implemented in WRF-Hydro-iso. It is highlighted that the model code lines involving fractionation calculations are featured with switches, which allows to turn on or off each specific fractionation process and facilitate a sensitivity analysis as in Christner et al. (2018).

2.4. Isotopic Fractionation With Sea Surface Evaporation

Assuming that the near-surface water vapor is in isotopic equilibrium with sea surface water, as in Merlivat and Jouzel (1979), the following bulk aerodynamic formula is applied for the computation of the isotopic evaporation flux at the sea surface E_{sea}^{iso} in WRF-Hydro-iso:

$$E_{sea}^{iso} = \alpha_k C_{sea} \left(\underbrace{\frac{r_{sea}^{iso}}{\alpha_{v/l}^{iso}\left(T_{sea}\right)} q_{sat}\left(T_{sea}\right)}_{q_{sat}^{iso}\left(T_{sea}\right)} - q^{iso} \right) \tag{5}$$

where α_k is the kinetic fractionation factor, C_{sea} is the exchange coefficient at sea surface, $q_{\mathrm{sat}}^{\mathrm{iso}}$ is the saturated mixing ratio of the isotopic water vapor at sea surface temperature T_{sea}, and q^{iso} is the mixing ratio of the isotopic water vapor at the first atmospheric level above the surface. $q_{\mathrm{sat}}^{\mathrm{iso}}$ is defined as the saturated mixing ratio of water vapor q_{sat} weighted by the ratio between the isotopic ratio of sea surface water $r_{\mathrm{sea}}^{\mathrm{iso}}$ and the isotopic equilibrium fractionation factor for vapor-to-liquid water phase change $\alpha_{v/l}^{\mathrm{iso}}$.

Concerning isotopic parameters in Equation 5, α_k is calculated as a function of wind velocity following the Merlivat and Jouzel's (1979) approach, as detailed in Nusbaumer et al. (2017); $r_{\mathrm{sea}}^{\mathrm{iso}}$ is set to the literature values mentioned, for example, in Hoffmann et al. (1998), that are 1.0005 for $^{1}H_2\,^{18}O$ and 1.004 for $^{1}H\,^{2}H\,^{16}O$; and the $\alpha_{v/l}^{\mathrm{iso}}$ coefficients for $^{1}H_2\,^{18}O$ and $^{1}H\,^{2}H\,^{16}O$ are obtained with the empirical functions of temperature from Majoube (1971b).

2.5. Isotopic Fractionation With Land Surface Evaporation

In Noah-MP (Niu et al., 2011), the land surface evaporation is divided into direct evaporation E_{dir} from bare ground and vegetated ground, canopy evaporation E_{can} from intercepted water at the canopy of the vegetation, and transpiration E_{tr} from plants and trees. Direct and canopy evaporation are usually assumed to fractionate water isotopologues, but not transpiration (e.g., Gat, 1996). Isotopic fractionation occurring during direct and canopy evaporation can be assessed with a formula similar to that for sea surface evaporation in Equation 5, as done, for example, by Haese et al. (2013).

In the case of Noah-MP with WRF-Hydro-iso, the following bulk aerodynamic formulas are applied for the computation of the isotopic direct and canopy evaporation fluxes $E_{\mathrm{dir}}^{\mathrm{iso}}$ and $E_{\mathrm{can}}^{\mathrm{iso}}$:

$$E_{dir}^{iso} = \alpha_k C_{g,b} \left(\underbrace{\frac{r_{\theta 1}^{iso}}{\alpha_{v/l}^{iso}\left(T_{g,b}\right)} e_{sat}\left(T_{g,b}\right)}_{e_{sat}^{iso}\left(T_{g,b}\right)} h_g - e_{air}^{iso} \right) + \alpha_k C_{g,v} \left(\underbrace{\frac{r_{\theta 1}^{iso}}{\alpha_{v/l}^{iso}\left(T_{g,v}\right)} e_{sat}\left(T_{g,v}\right)}_{e_{sat}^{iso}\left(T_{g,v}\right)} h_g - e_{ac}^{iso} \right) \tag{6}$$

and

$$E_{can}^{iso} = \alpha_k C_v \left(\underbrace{\frac{r_{Wcan,liq}^{iso}}{\alpha_{v/l}^{iso}\left(T_v\right)} e_{sat}\left(T_v\right)}_{e_{sat}^{iso}\left(T_v\right)} - e_{ac}^{iso} \right) \tag{7}$$

where α_k is the above-mentioned kinetic fractionation factor from Merlivat and Jouzel (1979); $C_{g,b}$, $C_{g,v}$, and C_v are the exchange coefficients at bare ground, vegetated ground, and in the canopy vegetation, respectively; $e_{\mathrm{sat}}^{\mathrm{iso}}$ is the saturated pressure of isotopic water vapor computed at bare ground temperature $T_{g,b}$, vegetated ground temperature $T_{g,v}$, and vegetation canopy temperature T_v; h_g is the relative humidity of the air in the surface soil pore space; $e_{\mathrm{air}}^{\mathrm{iso}}$ and $e_{\mathrm{ac}}^{\mathrm{iso}}$ are the isotopic water vapor pressures at the first atmospheric level and in the canopy air, respectively. In Equations 6 and 7, $e_{\mathrm{sat}}^{\mathrm{iso}}$ is expressed as a function of the saturated pressure of water vapor q_{sat}, the isotopic ratio of either liquid soil moisture in the first soil layer $r_{\theta 1}^{\mathrm{iso}}$ or liquid canopy water $r_{\mathrm{Wcan,liq}}^{\mathrm{iso}}$, and the above-mentioned isotopic equilibrium fractionation factor $\alpha_{v/l}^{\mathrm{iso}}$.

In the following, we introduce the variable E_{ev} computed as the sum of E_{dir} and E_{can}, which evaluates the *fractionating* land surface evaporation. The isotopic composition of E_{ev} is obtained with $E_{\mathrm{ev}}^{\mathrm{iso}}$, computed as the sum of $E_{\mathrm{dir}}^{\mathrm{iso}}$ and $E_{\mathrm{can}}^{\mathrm{iso}}$. The *nonfractionating* component of land surface evaporation is obtained with the

transpiration E_{tr}. Finally, the sum of E_{ev} and E_{tr} constitutes the land surface evaporation E, and the sum of E_{ev}^{iso} and E_{tr}^{iso} gives the isotopic land surface evaporation E^{iso}.

2.6. Isotopic Fractionation With Cloud Droplet Condensation/Evaporation

Isotopic fractionation occurring during cloud droplet condensation/evaporation is usually considered to be in isotopic equilibrium, since condensed cloud droplets remain suspended in the air and stay in contact with the water vapor they originate from (e.g., Hoffmann et al., 1998). The isotopic equilibrium occurring between mixing ratios of water vapor q, isotopic water vapor q^{iso}, cloud water q_{cloud}, and isotopic cloud water q_{cloud}^{iso} is characterized as:

$$\frac{q_{cloud}^{iso} + \Delta q_{cond}^{iso}}{q_{cloud} + \Delta q_{cond}} = \alpha_{v/l}^{iso} \frac{q^{iso} - \Delta q_{cond}^{iso}}{q - \Delta q_{cond}} \tag{8}$$

where Δq_{cond} and Δq_{cond}^{iso} are the amounts of condensation of cloud water and of isotopic cloud water within a model time step, and $\alpha_{v/l}^{iso}$ is the above-mentioned isotopic equilibrium fractionation factor. It is noted that Equation 8 is also valid for negative Δq_{cond}, that is, when cloud droplets evaporate.

In the WSM6 microphysics scheme, the water variables are advanced each time step using water phase change amounts such as Δq_{cond}. In WRF-Hydro-iso, it is chosen to advance the isotopic water variables in a similar manner as the water variables, which requires that the formulation of Δq_{cond}^{iso} is given explicitly. Equation 8 yields the following expression for Δq_{cond}^{iso}:

$$\Delta q_{cond}^{iso} = \Delta q_{cond} + \frac{\alpha_{v/l}^{iso}\left(q_{cloud} + \Delta q_{cond}\right)\left(q^{iso} - \Delta q_{cond}\right) - \left(q_{cloud}^{iso} + \Delta q_{cond}\right)\left(q - \Delta q_{cond}\right)}{\alpha_{v/l}^{iso}\left(q_{cloud} + \Delta q_{cond}\right) + \left(q - \Delta q_{cond}\right)} \tag{9}$$

The advantage of Equation 9 is that it allows a straightforward implementation of isotopic water phase changes in the WSM6 microphysics scheme of WRF-Hydro-iso. Furthermore, Equation 9 ensures that Δq_{cond} and Δq_{cond}^{iso} are equal when $\alpha_{v/l}^{iso}$ is set to 1 and the isotopic water variables are equal to their corresponding water variables, which is a useful property for testing the conservation of water isotopologues in WRF-Hydro-iso.

2.7. Isotopic Fractionation With Ice Nuclei Generation and Deposition

Isotopic fractionation occurring during ice nuclei generation as well as during ice, snow, or graupel deposition is usually considered as instantaneous extraction, which means that neither ice nor snow or graupel stay in contact with the water vapor it originates from (e.g., Hoffmann et al., 1998). Referring to ice, snow, or graupel as solid hydrometeors, the relationship between mixing ratios of water vapor q, isotopic water vapor q^{iso}, solid hydrometeors q_{solid}, and isotopic solid hydrometeors q_{solid}^{iso} during an instantaneous extraction is expressed as:

$$\frac{\Delta q_{gen/dep}^{iso}}{\Delta q_{gen/dep}} = \underbrace{\alpha_{v/s}^{iso} \frac{S}{\alpha_{v/s}^{iso}\left(1 + \varepsilon_D\right)\left(S - 1\right) + 1}}_{\alpha_{ki}^{iso}} \frac{q^{iso} - \Delta q_{gen/dep}^{iso}}{q - \Delta q_{gen/dep}} \tag{10}$$

where $\Delta q_{gen/dep}$ and $\Delta q_{gen/dep}^{iso}$ are the amounts of generation/deposition of solid hydrometeors and of isotopic solid hydrometeors within a model time step, and α_{ki}^{iso} is the isotopic fractionation factor including a kinetic effect caused by supersaturation during deposition (Jouzel & Merlivat, 1984). Following Jouzel and Merlivat (1984), α_{ki}^{iso} is calculated as a function of the supersaturation ratio S, the relative difference in isotopic molecular diffusivity ε_D defined in Merlivat and Jouzel (1979), and the isotopic equilibrium fractionation factor associated with vapor-to-solid water phase change $\alpha_{v/s}^{iso}$, empirically obtained by Majoube (1971a) for $^{1}H_2\,^{18}O$ and by Merlivat and Nief (1967) for $^{1}H\,^{2}H^{16}O$. It is noted that Equation 10 is not valid when $\Delta q_{gen/dep}$ is negative, as isotopic fractionation is generally assumed not to occur during the sublimation of solid hydrometeors (e.g., Pfahl et al., 2012).

From Equation 10, the following expression for $\Delta q_{gen/dep}^{iso}$ is derived:

$$\Delta q_{gen/dep}^{iso} = \Delta q_{gen/dep} + \frac{\alpha_{ki}^{iso}\Delta q_{gen/dep}\left(q^{iso} - \Delta q_{gen/dep}\right) - \Delta q_{gen/dep}\left(q - \Delta q_{gen/dep}\right)}{\alpha_{ki}^{iso}\Delta q_{gen/dep} + \left(q - \Delta q_{gen/dep}\right)} \quad (11)$$

This formulation has the same advantages as Equation 9, which are identical $\Delta q_{gen/dep}$ and $\Delta q_{gen/dep}^{iso}$ when α_{ki}^{iso} is set to 1 and the isotopic water variables are equal to their corresponding water variables, and the fact that it allows implementing the isotopic water phase changes in a similar manner as the water phase changes in the WSM6 microphysics scheme of WRF-Hydro-iso.

2.8. Isotopic Fractionation With Rain Droplet Evaporation

Isotopic fractionation occurring during rain droplet evaporation is implemented following the innovative method of Nusbaumer et al. (2017). This method assumes that only a fraction of the evaporated rain water is in isotopic equilibrium such as that described by Equation 9, and that this equilibrated fraction is determined as a function of raindrop fall velocity. The remaining fraction of evaporated rain water is assumed to evaporate without isotopic fractionation. The detailed set of equations to compute this isotopic fractionation process can be found in Nusbaumer et al. (2017).

3. Application

3.1. Driving Data

The selected data set of $^{1}H_{2}{}^{18}O$ and $^{1}H\,^{2}H^{16}O$ to drive WRF-Hydro-iso is obtained with the isotope-enabled version of the National Center for Atmospheric Research's Community Earth System Model Version 1 (iCESM1, Brady et al., 2019), which describes the fate of $^{1}H_{2}{}^{18}O$ and $^{1}H\,^{2}H^{16}O$ within the isotope-enabled Community Atmosphere Model Version 5 (iCAM5, Nusbaumer et al., 2017) and the isotope-enabled Community Land Model Version 4 (iCLM4, Wong et al., 2017). For this study, iCESM1 has been run for a 10-year period using the so-called FiC5 compset, which is the present-day iCAM/iCLM default run setup with prescribed sea-surface temperatures, isotopic ratio of sea surface water, and sea-ice extent (e.g., Nusbaumer et al., 2017), using a resolution of 0.9° in latitude and 1.25° in longitude, and 30 vertical levels up to 3 hPa.

The generated iCESM1 data set contains atmospheric and land surface variables at a six-hourly interval. Of particular interest are the iCESM1 isotopic water variables such as the atmospheric mixing ratios of isotopic water vapor, isotopic snow cover depth, and isotopic soil moisture, each of these isotopic water variables being normalized by the VSMOW concentration ratio as in WRF-Hydro-iso. The iCESM1 atmospheric variables have been saved on the 27 pressure levels of the ERA5 reanalyses (Hersbach et al., 2020), ranging from 1,000 hPa at the bottom to 1 hPa at the top.

In order to reduce the impact of potential climate biases in iCESM1 and to improve the resolution of the driving data set, it is chosen not to directly drive WRF-Hydro-iso with the iCESM1 data set, but instead to set the initial and lateral boundary conditions of the usual land-atmospheric variables in WRF-Hydro-iso with the ERA5 reanalyses. The ERA5 reanalyses, which are provided at a six-hour interval on a regular latitude-longitude grid with a resolution of 0.25° × 0.25°, allow to set the initial and lateral boundary condition of atmospheric-wind, temperature, pressure, and water vapor, and to set the initial condition of the snow cover height, soil moisture, and soil temperature.

The iCESM1 data set is used to derive climatological monthly δ-values of isotopic concentrations for the atmospheric water vapor, snow cover height, and soil moisture. The monthly iCESM1 climatological isotopic δ-values are combined with the six hourly ERA5 variables in order to generate a hybrid iCESM1/ERA5 data set of isotopic atmospheric water vapor, isotopic snow cover height, and isotopic soil moisture, which is suitable for setting the initial and lateral boundary conditions of the isotopic water variables in WRF-Hydro-iso.

3.2. Model Setup

The same WRF-Hydro-iso settings are used for the simulations for Europe and Southern Africa. An outer domain with a 10 km grid-spacing, covering an area of 3,600 × 5,000 km, is employed to downscale the hybrid iCESM1/ERA5 driving data. An inner domain with a 5 km grid-spacing and covering an area of

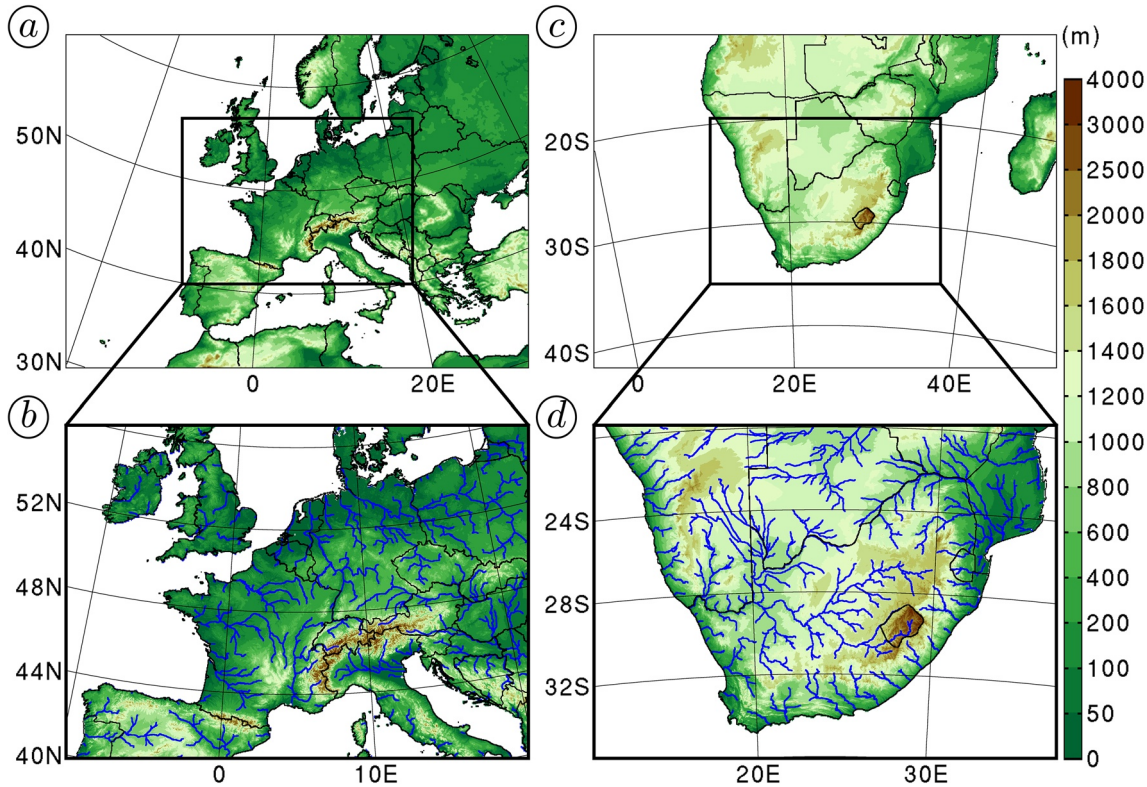

Figure 1. (a and b) Terrain elevation of the simulations' outer domain (a) and inner domain (b) for Europe, given in meters above sea level. The solid black lines delineate the political boundaries and the solid blue lines in (b) indicate the river channels with Strahler stream order equal to or above 6. (c and d) As in (a and b), except for Southern Africa.

1,800 × 2,500 km is nested within this outer domain using a one-way nesting approach, as illustrated in Figure 1. The equations of motion are resolved with a time step of 50 s for the outer domain and 25 s for the inner domain, for a time period of 12 years extending from 2001 to 2012. The first 2 years are considered as model spin-up period for the terrestrial variables of the model, so that only the last 10 years are retained for the analysis. Model outputs are saved at a daily interval.

The same set of physics schemes is used for both domains, including the long and short-wave radiative fluxes schemes of Mlawer et al. (1997) and Dudhia (1989), the WSM6 microphysics scheme, the ACM2 atmospheric turbulence scheme, and the Noah-MP LSM. The choice of WSM6, ACM2, Noah-MP, and waiving of cumulus parameterization is a constraint of WRF-Hydro-iso in its current version. It is noted that this physics setup with a grid-spacing of 5 km proved to give reasonable results for summer precipitation in Europe and West Africa (Arnault et al., 2021).

The aim of the outer domain is to set the hybrid iCESM1/ERA5 lateral boundary forcing far from the study region, with the constraint to use the above-detailed WRF-Hydro-iso physics setup in order to correctly prescribe the lateral boundary condition of the inner domain's isotopic water variables. The reason for choosing a grid-spacing of 10 km for the outer domain is that it also gives reasonable results (not shown). In the following, all presented model results refer to the inner domain.

In WRF-Hydro-iso, the inner domain can be coupled with a subgrid to compute overland and subsurface water flow (Gochis et al., 2018). For both Europe and Southern Africa, the subgrid is generated with the WRF-Hydro Pre-processing Tool and using the digital elevation data from the hydrological data and maps based on Shuttle Elevation Derivatives at Multiple Scales (HydroSHEDS) data base (Lehner et al., 2008), with a 500 m grid spacing and a minimal number of pixels to define a stream set to 4. The locations of the main river channels obtained with this method are displayed in Figure 1. In case lateral terrestrial water flow is considered in the WRF-Hydro-iso setup, the surface ponded water and liquid soil moisture variables

Table 1
WRF-Hydro-Iso Setup Options Considered for the Sensitivity Analysis

	sim1	sim2	sim3
Sea surface fractionation	x	x	x
Atmospheric fractionations	x	x	x
Surface evaporation fractionations		x	x
Overland and subsurface flow			x

from the inner domain grid are disaggregated to the finer subgrid, routed at the surface and in the subsurface, and aggregated back to the inner domain grid at each time step.

3.3. Observational Data Sets

For assessing the realism of the simulated climate, station-based gridded data sets of land surface evaporation, precipitation, and temperature are employed. For the case of Europe, we use the FLUXNET Model Tree Ensemble (MTE, Jung et al., 2009, 2010) global data set of monthly sums of land surface evaporation at a spatial resolution of 0.5°, and the European Climate Assessment & Data set project (EOBS, Haylock et al., 2008) data set of daily precipitation sums and daily averaged temperature at a spatial resolution of 0.25°. For the case of Southern Africa, we also use the MTE land surface evaporation, as well as the climate hazards infrared precipitation with stations (Funk et al., 2015) data set of daily precipitation sums available within the latitudinal band between 50°S and 50°N at a spatial resolution of 0.05°, and the Climate Research Unit (CRU, Harris et al., 2014) global data set of monthly averaged temperature at a spatial resolution of 0.5°.

The realism of the simulated isotopic concentrations is assessed with the GNIP data set of precipitation and precipitation isotopic concentrations $\delta_P{}^{18}\mathrm{O}$ and $\delta_P{}^{2}\mathrm{H}$ (IAEA/WMO, 2020). GNIP stations observations are monthly average. These monthly values are used to derive climatological values of $\delta_P{}^{18}\mathrm{O}$ and $\delta_P{}^{2}\mathrm{H}$ for the entire period of observation at each station, which are compared to the simulated isotopic concentrations in precipitation at the nearest grid point. A list of the stations considered for Europe and Southern Africa is detailed in Tables 2 and 3. It is noted that the selected stations in Tables 2 and 3 have an altitude close to that in the model, with a difference smaller than ±500 m, to ensure a fair comparison between modeled and observed isotopic concentrations.

3.4. Sensitivity Analysis Strategy

In order to evaluate the benefit of using a coupled atmospheric-hydrological modeling system for representing water isotopologues, we compare two effects on isotopic concentrations, namely the effect of lateral terrestrial water flow and the effect of land surface evaporation fractionation. This sensitivity analysis is achieved by running the model three times each for Europe and for Southern Africa, using the following setups as summarized in Table 1: (sim1) Atmospheric fractionation processes, (sim2) Atmospheric fractionation processes + Land surface evaporation fractionation processes, and (sim3) Atmospheric fractionation processes + Land surface evaporation fractionation processes + Lateral terrestrial water flow.

It is noted that sim1 and sim2 are identical in terms of land-atmospheric variables, with differences only in isotopic concentrations. Sim3, which includes lateral terrestrial water flow, provides a different realization of the land-atmosphere system. It is assumed that the study period is long enough to mostly smooth random fluctuations in the model, so that the study period-averaged differences between sim3 and the other simulation results are mainly due to the consideration of lateral terrestrial water flow.

The comparison between simulation results from sim1 and sim2 allows to quantify the contribution of land surface evaporation fractionation on any model variable X with:

$$\Delta_X^{Efrac} = \left(X\right)_{sim2} - \left(X\right)_{sim1} \tag{12}$$

Similarly, the comparison between simulation results from sim2 and sim3 allows to quantify the contribution of lateral terrestrial water flow with:

$$\Delta_X^{Hydro} = \left(X\right)_{sim3} - \left(X\right)_{sim2} \tag{13}$$

Specifically, the differences $\Delta_X^{\mathrm{Efrac}}$ and $\Delta_X^{\mathrm{Hydro}}$ are evaluated for precipitation P, land surface evaporation E, rootzone soil moisture volumetric ratios θ_r, and for their respective isotopic concentration ratios δ_P^{iso}, δ_E^{iso}, and $\delta_{\theta_\mathrm{r}}^{\mathrm{iso}}$. For clarification, θ_r is the averaged soil moisture of the soil layers within the rootzone, and the

Table 2
List of Global Network of Isotopes in Precipitation Stations of Stable Water Isotopologue Measurements in Precipitation for Europe

Country	Station name	Latitude, longitude	Period of data availability
Austria	Vienna	48.25°N, 16.36°E	1961–2018
Belgium	Liege	50.70°N, 5.47°E	1966–1970
Croatia	Zagreb	45.81°N, 15.97°E	1980–1995
Czechia	Prague	50.12°N, 14.39°E	2012–2018
France	Avignon	43.95°N, 4.82°E	1997–2013
France	Brest-Plouzane	48.36°N, 4.57°W	1996–2002
France	Cestas-Pierroton	44.74°N, 0.77°W	2007–2018
France	Dax	43.68°N, 1.07°W	1999–2004
France	Draix	44.13°N, 6.33°E	2004–2012
France	Orleans-la-source	47.83°N, 1.94°E	1996–2008
Germany	Artern	51.37°N, 11.29°E	1997–2013
Germany	Bad Salzuflen	52.10°N, 8.75°E	1978–2011
Germany	Berlin	52.47°N, 13.40°E	1978–2012
Germany	Braunschweig	52.29°N, 10.45°E	1978–2012
Germany	Cuxhaven	53.87°N, 8.71°E	1978–2012
Germany	Emmerich	51.83°N, 6.25°E	1978–2012
Germany	Fehmarn	54.53°N, 11.06°E	1997–2013
Germany	Garmisch-Partenkirchen	47.48°N, 11.06°E	1978–2013
Germany	Goerlitz	51.16°N, 14.95°E	1997–2013
Germany	Hof-Hohensaas	50.31°N, 11.88°E	1983–2013
Germany	Kahler Asten	51.18°N, 8.49°E	1997–2013
Germany	Karlsruhe	49.04°N, 8.37°E	1981–2012
Germany	Koblenz	50.34°N, 7.60°E	1981–2012
Germany	Konstanz	47.68°N, 9.19°E	1978–2013
Germany	Passau-Fuerstenzell	48.55°N, 13.36°E	1997–2013
Germany	Regensburg	49.04°N, 12.10°E	1978–2013
Germany	Schleswig	54.53°N, 9.55°E	1998–2013
Germany	Trier	49.75°N, 6.66°E	1978–2013
Germany	Wasserkuppe Rhoen	50.50°N, 9.94°E	1978–2013
Ireland	Valentia Observatory	51.93°N, 10.25°W	1960–2015
Italy	Brasimone	44.09°N, 11.08°E	1971–1976, 1985–1986
Italy	Genoa	44.42°N, 8.85°E	1961–1965, 1973–2001
Netherlands	Groningen	53.23°N, 6.55°E	1964–2012
Poland	Krakow	50.06°N, 19.85°E	1975–2016
Slovakia	Liptovsky Mikulas	49.10°N, 19.59°E	1992–2011, 2013–2016
Slovenia	Ljubljana	46.10°N, 14.60°E	1984–2010
Spain	A Coruna	43.37°N, 8.42°W	2000–2016
Spain	Santander	43.49°N, 3.80°W	2000–2010, 2012–2015
Switzerland	Bern	46.95°N, "7.44°E	1983–1992, 2002–2008
United Kingdom	Keyworth	52.88°N, 1.08°W	1985–1996
United Kingdom	Wallingford	51.60°N, 1.10°W	1981–2015

Table 3
List of Global Network of Isotopes in Precipitation Stations of Stable Water Isotopologue Measurements in Precipitation for Southern Africa

Country	Station name	Latitude, longitude	Period of data availability
Namibia	Windhoek	22.95°S, 17.15°E	1961–1975
South Africa	Pretoria	25.73°S, 28.18°E	1961–1875, 1996–2000
South Africa	Cape Town Airport	33.97°S, 18.60°E	1961–1974, 1996–2001, 2009–2012

depth of the rootzone is a distributed parameter prescribed as a function of land use classes from the moderate resolution imaging spectroradiometer (MODIS) land cover map (Friedl et al., 2002).

Finally, it is highlighted that the reconstruction of paleo-precipitation from isotopic concentrations is based on proxy records such as plant wax deuterium concentrations $\delta_{\text{wax}}{}^{2}\text{H}$ measured in the sediments (e.g., Dupont et al., 2013; Herrmann et al., 2017; Schefuß et al., 2011). However, the relationship between $\delta_P{}^{2}\text{H}$ and $\delta_{\text{wax}}{}^{2}\text{H}$ may be altered by processes having occurred in the rootzone, so that $\delta_{\text{wax}}{}^{2}\text{H}$ may be closer to $\delta_{\theta_r}{}^{2}\text{H}$ rather than $\delta_P{}^{2}\text{H}$. In order to relate our study to the paleo-precipitation reconstruction with $\delta_{\text{wax}}{}^{2}\text{H}$, it is chosen to focus our sensitivity analysis of isotopic concentrations to $\Delta_{\delta^2\text{H}}^{Efrac}$ and $\Delta_{\delta^2\text{H}}^{\text{Hydro}}$, and to highlight the differences between $\delta_P{}^{2}\text{H}$ and $\delta_{\theta_r}{}^{2}\text{H}$. In particular, the overall contribution of the processes altering $\delta_{\theta_r}{}^{2}\text{H}$ after precipitation has reached the land surface, including land surface evaporation and soil water transport in the rootzone, is evaluated with:

$$\Delta_{\delta^2 H}^{soil} = \left(\delta_{\theta_r}{}^{2}H\right)_{sim3} - \left(\delta_P{}^{2}H\right)_{sim3} \tag{14}$$

4. Climate Modeling Results

4.1. Comparison to Observation—Land Averaged Time Series

Land surface evaporation, precipitation, and temperature results from the WRF-Hydro-iso simulations are evaluated with land-averaged climatological monthly time series in Figure 2. Europe and Southern Africa are characterized by an annual cycle of land surface evaporation and temperature with maxima in summer. In Southern Africa, precipitation follows a similar annual cycle, in contrast to Europe where precipitation remains relatively high all year long. On average, the European domain is characterized by a mean precipitation of 2.1 mm/day and a mean temperature of 283 K, whereas the Southern African domain experiences a much drier and warmer climate with a mean precipitation of 1.1 mm/day and a mean temperature of 293 K.

Figure 2 shows the good correspondence between modeled and observed climatological monthly variations. Concerning modeled land surface evaporation in Figures 2a and 2d, there is a general underestimation almost all year long, with a land surface evaporation mean bias of −15% for Europe and −25% for Southern Africa. Such negative mean biases could be related to inaccurate land use spatial information in Noah-MP, to a lack of modeled precipitation in the case of Southern Africa, and potential uncertainties in the observational data set as well (e.g., Jung et al., 2009).

Concerning the modeled precipitation in Europe displayed in Figure 2b, there is an overestimation from autumn to spring, leading to a precipitation mean bias of +15%. Such a cold season precipitation overestimation was also found by Prein et al. (2016) with regional climate models employing a spatial resolution of ∼12.5 km. In Southern Africa, there is a precipitation underestimation from mid-summer to mid-autumn, as shown in Figure 2e, leading to a precipitation mean bias of −10%. This is an opposite situation in comparison to other regional climate models employing spatial resolutions of ∼50 and 9 km, which generally simulate relatively high wet biases in the central and eastern part of Southern Africa (Kalognomou et al., 2013; Ratna et al., 2014). Crétat et al. (2012) demonstrated the uncertainty in simulated Southern African precipitation with respect to modeled physics, which shows that the Southern African precipitation mean bias obtained in this study is in the range of state-of-the-art models' biases (e.g., Crétat et al., 2012).

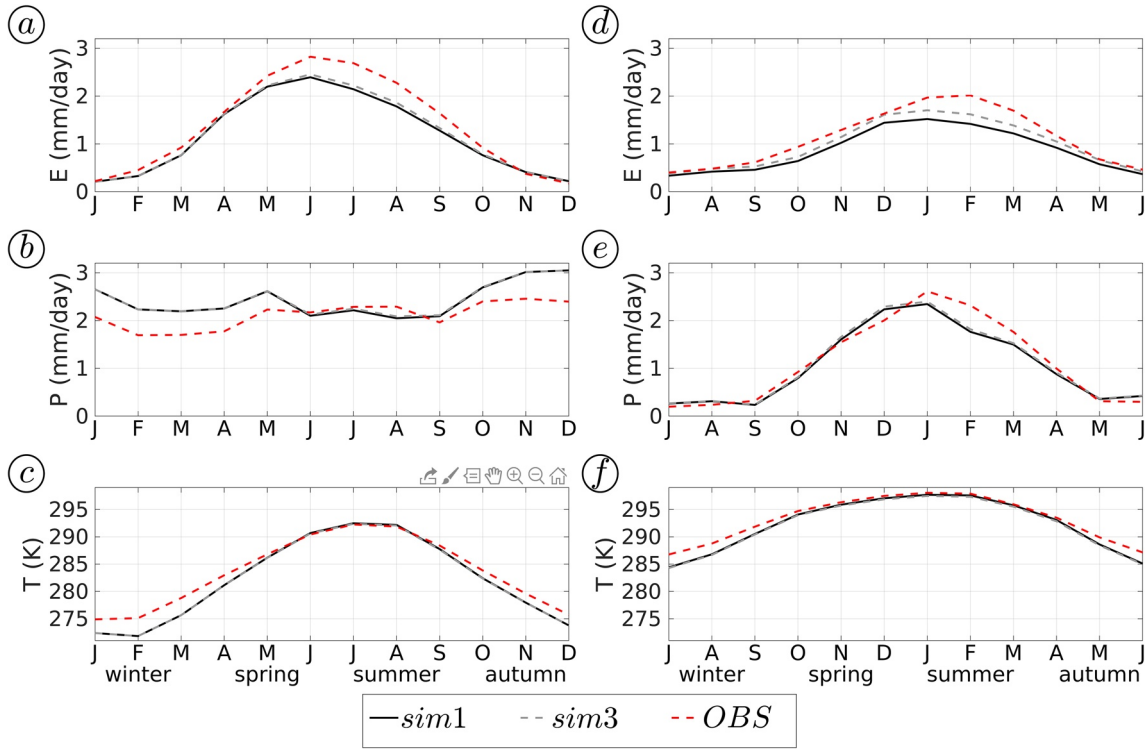

Figure 2. (a and b) Climatological time series for Europe of modeled and observational (a) land surface evaporation, (b) precipitation, and (c) temperature, computed as a series of monthly mean values for the period 2003–2012 and spatially averaged over the inner domain. Observational data set details are provided in Section 3.3. The *x*-axis gives the time in months from January to December, each month being indicated with its first letter. The *y*-axis gives the water flux scale in mm/day for (a and b) and the temperature scale in K for (c). (d–f) As in (a–c), except for Southern Africa and with the *x*-axis indicating the months from July to June. The aim of visualizing Southern African results from July to June is to have an *x*-axis spawning from winter to autumn, as in the case of Europe.

With respect to temperature in Figures 2c and 2f, there is a clear underestimation from late autumn to early spring, with a temperature mean bias of −1.4 K for Europe and −0.7 K for Southern Africa. According to the study of Haiden et al. (2018) for Europe, such a cold mean bias could be related to an underestimation of cloud cover during nighttime in winter, at least for Europe.

Figure 2 further displays the differences between model results from simulations with or without lateral terrestrial water flow. For Europe, lateral terrestrial water flow increases the mean land surface evaporation by +1.2% and mean precipitation by +0.5%, while it decreases the summer temperature by −0.1 K. For Southern Africa, lateral terrestrial water has a much larger effect as it increases the mean land surface evaporation by +10.7% and mean precipitation by +2.4%, while it decreases the summer temperature by −0.2 K. This wetting and cooling effect is related to the fact that the consideration of lateral terrestrial water flow generally increases the soil water storage and land surface evaporation (e.g., Fersch et al., 2020; Rummler et al., 2019; Zhang et al., 2019). However, these differences are much smaller than the biases-to-observations, except for the land surface evaporation in Southern Africa, which is much improved when the lateral terrestrial water flow is considered. This latter result suggests that the WRF model underestimation of land surface evaporation for Southern Africa is related to an underestimation of soil water storage, which can be partially mitigated with the consideration of lateral terrestrial water flow. The impact of lateral terrestrial water flow on model results is further discussed in Section 4.4.

4.2. Comparison to Observation—Multi-Year Averaged Maps

Land surface evaporation, precipitation, and temperature results from the WRF-Hydro-iso simulations are further evaluated with multi-year averaged maps in Figures 3–5, respectively.

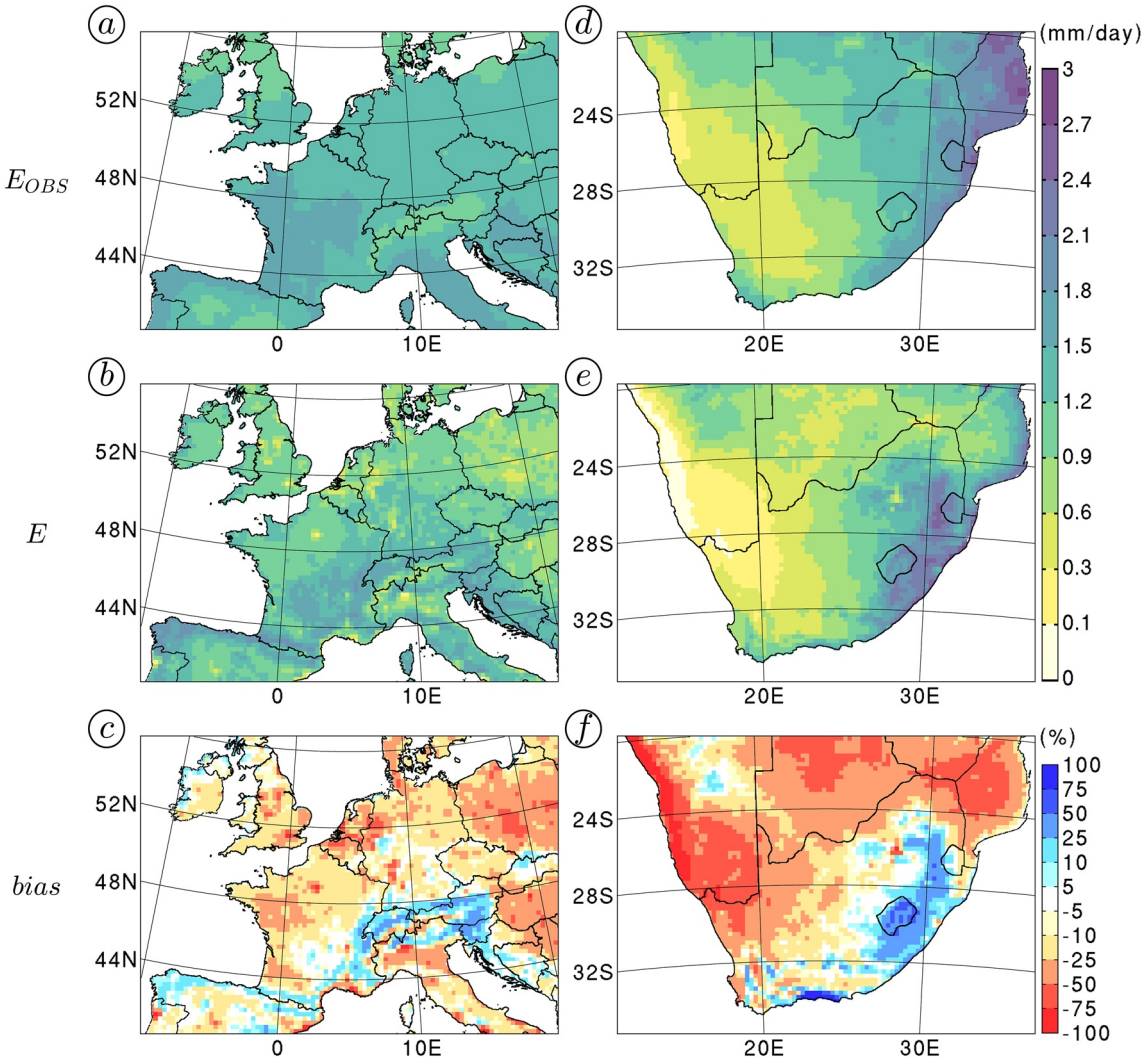

Figure 3. (a and b) Maps for Europe of observational land surface evaporation E_{OBS} and modeled land surface evaporation E from sim1, temporally averaged for the period from 2003 to 2012 and given in mm/day. (c) Difference in % between E_{OBS} and E, computed as the percent difference relative to observation. (d–f) As in (a–c), except for Southern Africa. In all panels, the data have been resampled on a grid with a 25 km grid spacing for visualization purpose. This resampling is applied to all maps shown in the following figures.

According to the observational data set in Figures 3a and 3d, the multi-year averaged land surface evaporation is relatively homogeneously distributed over Europe with some lower values in the Alpine region, whereas in Southern Africa there is a well-defined west-east gradient similar to that in the precipitation map shown in Figure 4d. In comparison, WRF-Hydro-iso generates much less land surface evaporation in most regions, as shown in Figures 3b–3e and 3f, which indicates that the above-discussed negative mean bias in land surface evaporation concerns most areas of the simulations' domains. Nevertheless, at relatively high elevation, for example, above 1,500 m above sea level like in the Alpine region in Europe and near the East coast of Southern Africa, the land surface evaporation bias eventually becomes positive, which could be related to a radiation-elevation dependency (e.g., Blumthaler et al., 1997) not properly captured by the observational data set.

The spatial characteristics of the multi-year averaged precipitation are relatively well captured by WRF-Hydro-iso, with enhanced precipitation in the mountainous regions of Europe in Figures 4a and 4b, and with enhanced precipitation in the eastern coastal region of Southern Africa in Figures 4d and 4e. The bias maps in Figures 4c and 4f reveal that the model generally overestimates these regions' enhanced precipitation. Precipitation overestimation spreads almost all over the European domain, especially in the Southern

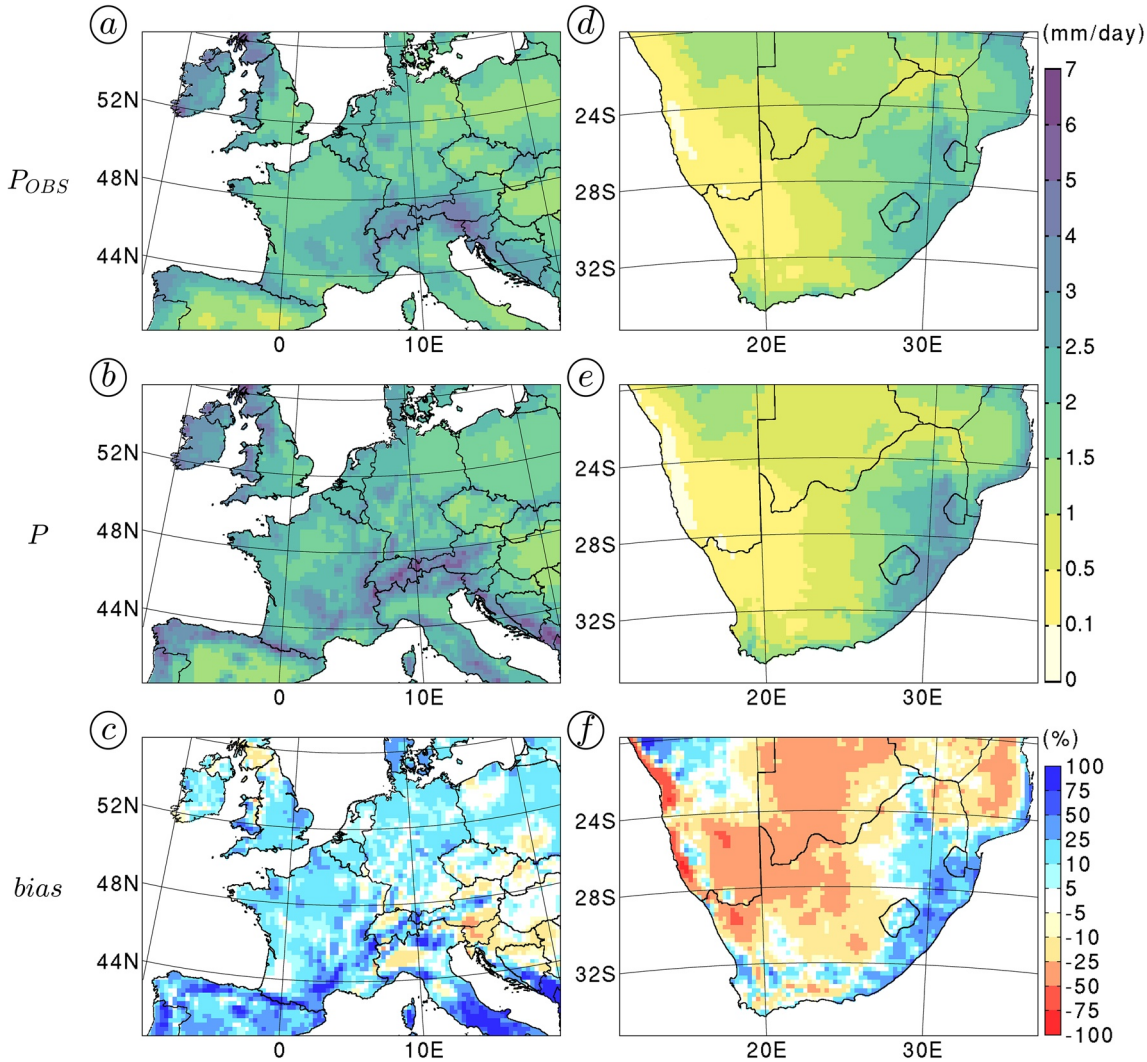

Figure 4. (a and b) Maps for Europe of observational precipitation P_{OBS} and modeled precipitation P from sim1, temporally averaged for the period from 2003 to 2012 and given in mm/day. (c) Difference in % between P_{OBS} and P, computed as the percent difference relative to observation. (d–f) As in (a–c), except for Southern Africa.

part of Italy where the observed precipitation amounts are relatively low. An opposite model behavior is obtained for Southern Africa, where the low precipitation amounts observed in the central and western regions are underestimated, resulting in the negative mean bias in precipitation mentioned above. This model discrepancy indicates a potential limitation of using the microphysics scheme alone at a 5 km grid-spacing to fully resolve the atmospheric systems producing precipitation in the most arid parts of Southern Africa, since other simulations using a cumulus parameterization generated a wet bias in these regions (Kalognomou et al., 2013; Ratna et al., 2014). Overall, the resemblance between precipitation bias maps in Figures 4c and 4f and land surface evaporation bias maps in Figures 3c and 3f suggests that the above-discussed positive biases in land surface evaporation at high elevations are also related to precipitation overestimations.

Finally, the spatial characteristics of the multi-year averaged temperature are also relatively well captured by WRF-Hydro-iso, with a well-defined temperature decrease with elevation, as shown for Europe in Figures 5a and 5b and for Southern Africa in Figures 5d and 5e. The bias maps in Figures 5c and 5f indicate that the above-discussed cold mean bias concerns almost all areas of the simulations' domains. The relatively high cold biases at high elevations are probably related to modeled features, which are not captured by the observational data sets. Still, temperatures along the northwest coast of Southern Africa are overestimated to a large extent, which may be related to the inability of the model to generate precipitation in this area.

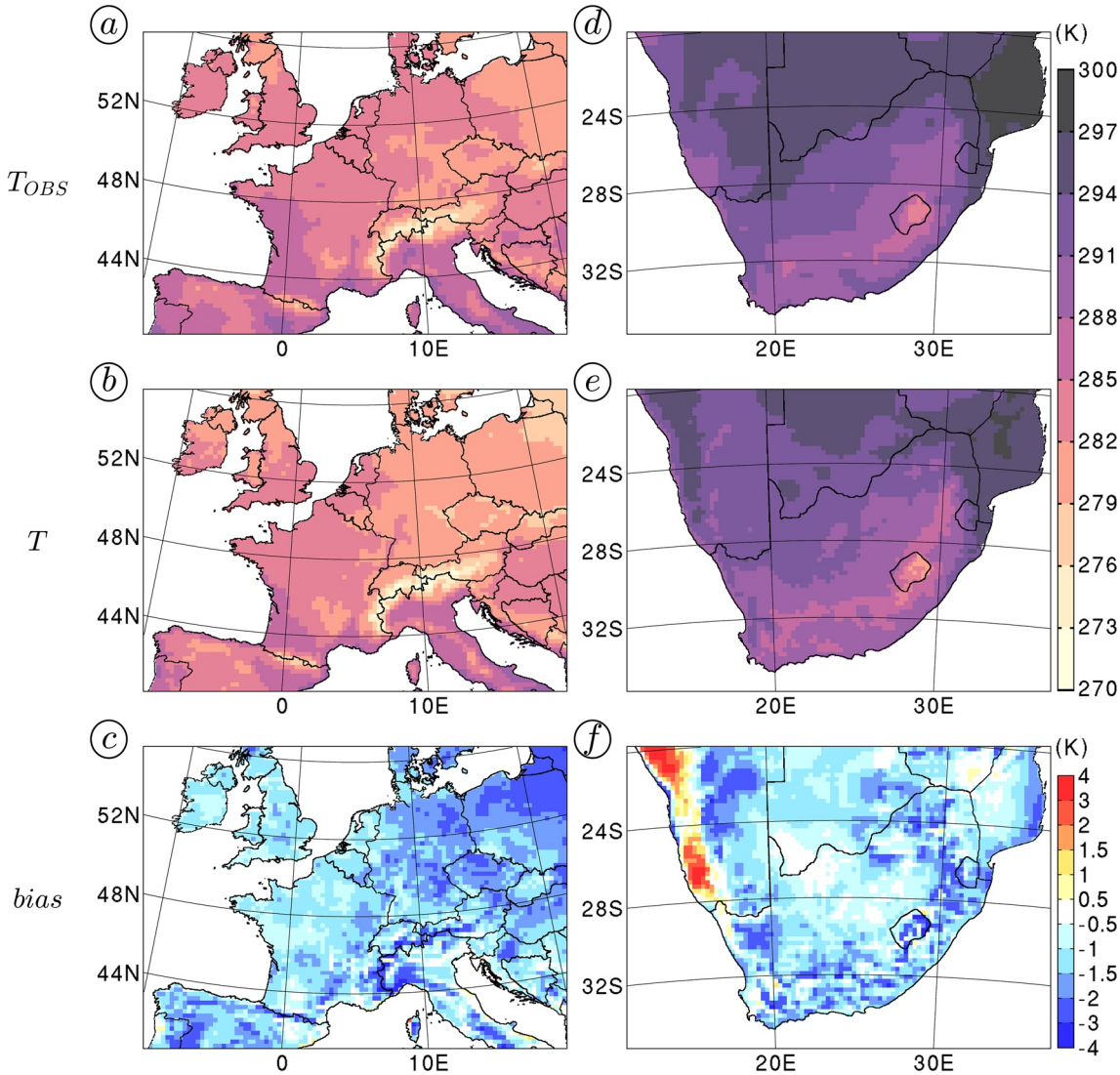

Figure 5. (a and b) Maps for Europe of observational temperature T_{OBS} and modeled temperature T from sim1, temporally averaged for the period from 2003 to 2012 and given in K. (c) Difference in K between T_{OBS} and T. (d–f) As in (a–c), except for Southern Africa.

Nevertheless, it is argued that WRF-Hydro-iso is able to generate realistic climate characteristics in Europe and Southern Africa, which gives us confidence in using this model for water isotopologue modeling.

4.3. Multi-Year Averaged Terrestrial Water Fluxes

The simulated terrestrial water fluxes are further detailed with multi-year averaged maps of rootzone soil moisture θ_r, fractionating surface evaporation E_{ev}, and transpiration E_{tr} in Figure 6.

In Europe, θ_r and E_{ev} are relatively homogeneously distributed whereas E_{tr} displays much larger spatial disparities as shown in Figures 6a–6c. In particular, most areas of low E_{tr} correspond to cropland areas, which indicates that the above-discussed negative bias in land surface evaporation could be related to an overestimation of cropland areas in the MODIS-derived land cover map at 5 km resolution. On average, the European precipitation is partitioned into 36% of fractionating surface evaporation, 12% of transpiration, and 52% of runoff. Locally, the ratio between runoff and precipitation, that is, the runoff coefficient, ranges from 0.2 in plain regions receiving the lowest precipitation amounts to 0.8 in mountainous regions receiving the highest precipitation amounts (not shown). The relatively high values of simulated runoff coefficients,

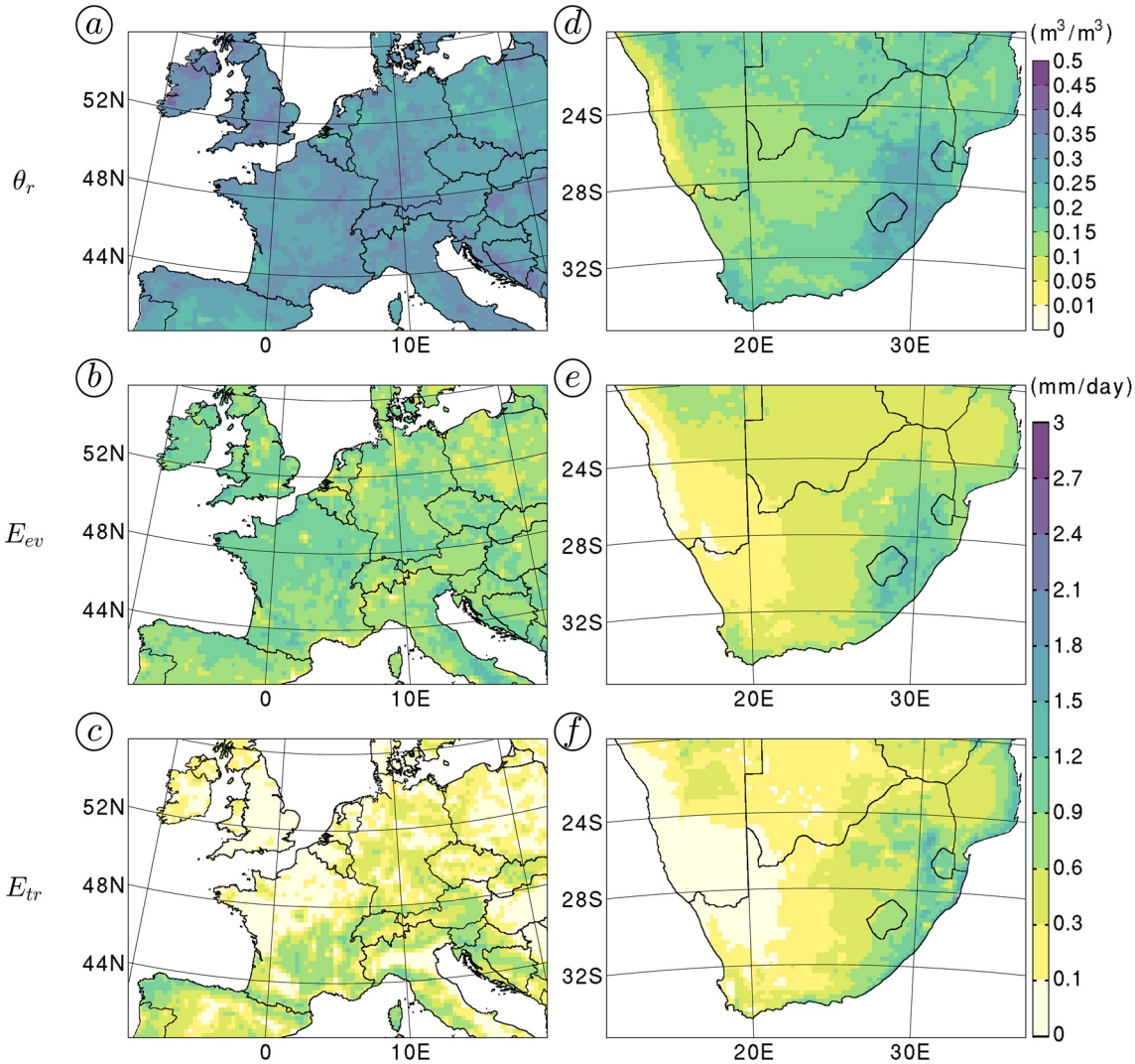

Figure 6. (a–c) Maps for Europe of modeled rootzone soil moisture θ_r, fractionating surface evaporation E_{ev}, and transpiration E_{tr} from sim1, temporally averaged for the period from 2003 to 2012 and given in m^3/m^3 for θ_r and in mm/day for E_{ev} and E_{tr}. (d–f) As in (a–c), except for Southern Africa.

in comparison to observations, for example, in the largest river basins in Germany (Zink et al., 2017), are assumed to be due to the precipitation overestimation in mountainous regions.

In Southern Africa, θ_r, E_{ev}, and E_{tr} display the above-mentioned west-east gradient, with enhanced values near the eastern coast, as shown in Figures 6d–6f. In comparison to Europe, θ_r displays much lower values. On average, the Southern African precipitation is partitioned into 48% of fractionating surface evaporation, 34% of transpiration, and 18% of runoff. The drier soils and the fact that most of the precipitation evaporates back to the atmosphere are related to the much warmer and drier climate in Southern Africa in comparison to Europe as illustrated in Figures 2–5.

4.4. Role of Lateral Terrestrial Water Flow

The role of lateral terrestrial water flow on terrestrial water fluxes is evaluated with multi-year averaged maps of $\Delta^{\text{Hydro}}_{\theta_r}$, $\Delta^{\text{Hydro}}_{E_{ev}}$, $\Delta^{\text{Hydro}}_{E_{tr}}$, and $\Delta^{\text{Hydro}}_{P}$ in Figure 7, these Δ^{Hydro} differences being defined according to Equation 13.

For Europe, Figure 7a confirms that the consideration of lateral terrestrial water flow generally increases soil water storage, except in regions with steep topography where the consideration of lateral terrestrial

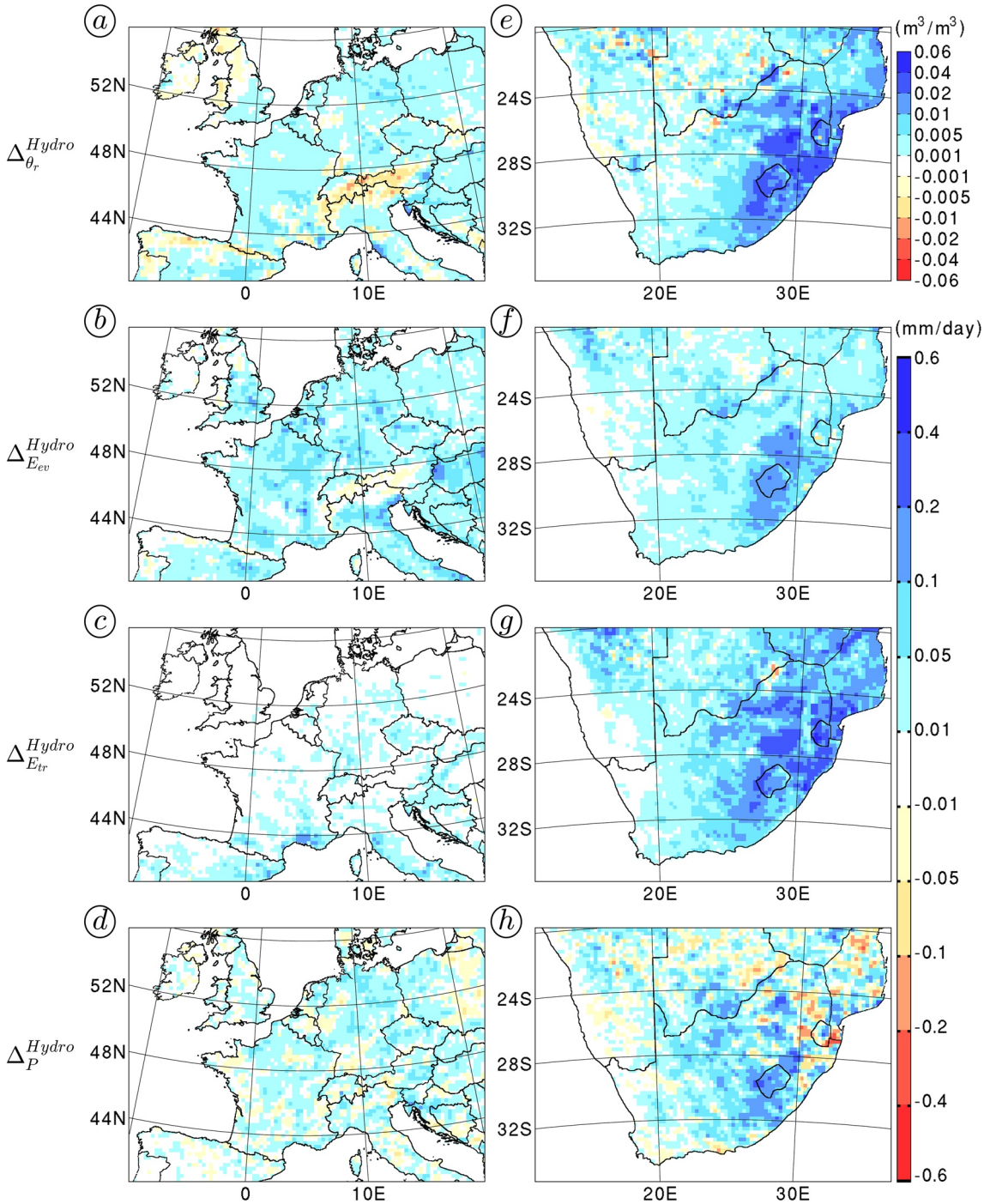

Figure 7. (a–d) Maps for Europe of the differences introduced by the consideration of lateral terrestrial water flow in rootzone soil moisture, fractionating surface evaporation, transpiration, and precipitation, namely $\Delta^{\mathrm{Hydro}}_{\theta_r}$, $\Delta^{\mathrm{Hydro}}_{E_{\mathrm{ev}}}$, $\Delta^{\mathrm{Hydro}}_{E_{\mathrm{tr}}}$, and $\Delta^{\mathrm{Hydro}}_{P}$, temporally averaged for the period from 2003 to 2012. The Δ^{Hydro} differences are computed according to Equation 13. (e–h) As in (a–d), except for Southern Africa.

water flow rather enhances the generation of surface runoff and reduces the soil water storage (e.g., Arnault et al., 2019). Figures 7b and 7c further show that the increase in land surface evaporation triggered by lateral terrestrial water flow is mainly supported by E_{ev}, which indicates that the direct evaporation is more soil moisture-limited than transpiration and therefore more sensitive to a soil moisture increase. Overall, the increase in land surface evaporation mostly increases precipitation through a land recycling process

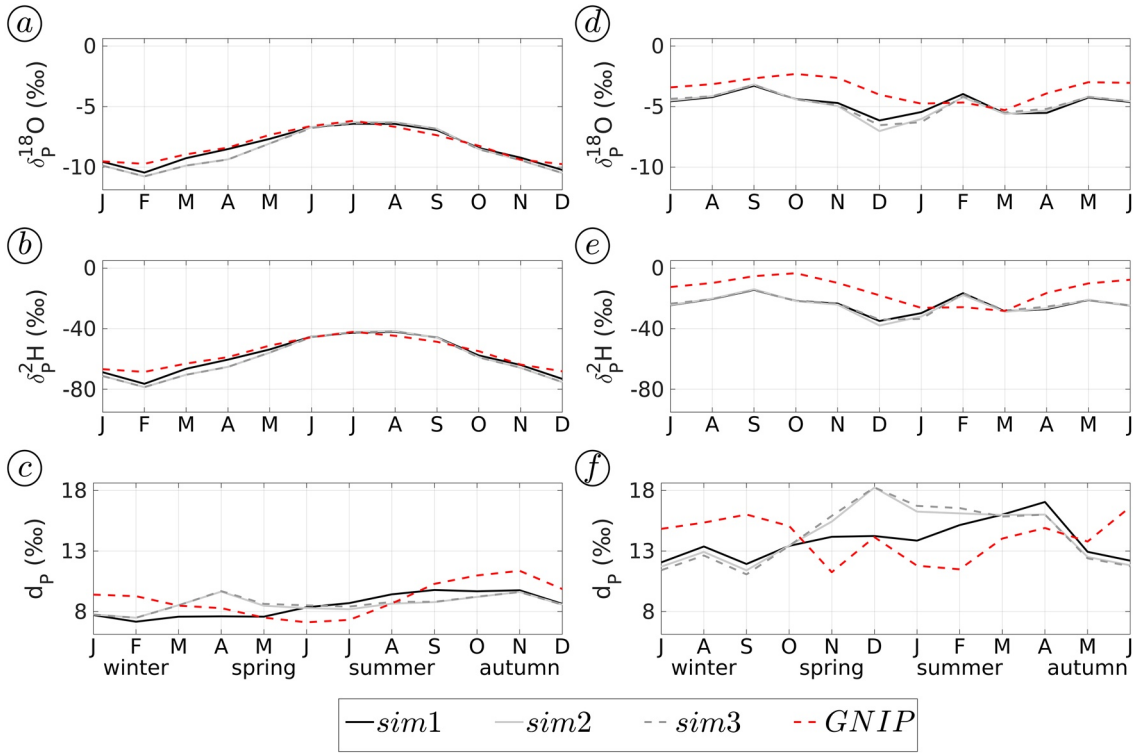

Figure 8. (a–c) Climatological time series for Europe of modeled and observational precipitation isotopic concentrations $\delta_P{}^{18}$O and $\delta_P{}^{2}$H and deuterium excess d_P from sim1, sim2, sim3, and GNIP, computed as a series of monthly mean values for the period 2003–2012 and averaged for the locations of the European stations listed in Table 2. The *y*-axis gives the isotopic concentration scale in in ‰. (d–f) As in (a–c), except for the stations listed in Table 3 for Southern Africa. In all panels, the *x*-axis indicates the months of the year as in Figure 2.

as displayed in Figure 7d. Following Arnault et al. (2021), it is assumed that the scattered negative values of Δ_P^{Hydro} in Figure 7d are related to modeled atmospheric randomnesses not fully smoothed in the 10-year mean simulations' results. On average for Europe, the consideration of lateral terrestrial flow induces +1.0% of fractionating surface evaporation, +0.2% of transpiration, +0.5% of precipitation, and −0.7% of runoff.

For Southern Africa, the increase in θ_r is much enhanced in comparison to Europe, especially in the eastern coastal region, which experiences the largest precipitation amounts. Figures 7f and 7g further show that the increase in land surface evaporation triggered by lateral terrestrial water flow is supported by both E_{ev} and E_{tr}, which indicates much drier soil conditions in Southern Africa and an enhanced sensitivity of transpiration to a soil moisture increase. Indeed, the additional soil water storage brought by the lateral terrestrial water flow mostly evaporates, as Southern Africa experiences a soil moisture-limited evaporation regime (e.g., Dirmeyer et al., 2012). This relatively large increase in land surface evaporation mostly increases precipitation as displayed in Figure 7h, with some visible patterns of modeled atmospheric randomnesses not fully smoothed by the 10-year mean, as in the case of Europe. On average for Southern Africa, the consideration of lateral terrestrial flow induces +3.6% of fractionating surface evaporation, +7.1% of transpiration, +2.4% of precipitation, and −8.3% of runoff.

5. Water Isotopologue Modeling Results

5.1. Comparison to Observation—Land Averaged Time Series

The model skill in reproducing the climatological precipitation isotopic concentrations $\delta_P{}^{18}$O and $\delta_P{}^{2}$H from the GNIP data set is evaluated with station-averaged climatological monthly time series in Figure 8. The deuterium excess $d_P = \delta_P{}^{2}\text{H} - 8\delta_P{}^{18}\text{O}$ (e.g., Craig, 1961) is also shown in Figure 8, in order to more specifically assess the kinetic effect associated with surface evaporation fractionation (e.g., Risi et al., 2016). Figure 8 displays model results from sim1, sim2, and sim3, as well as the GNIP data set, which allows to

evaluate the effect of surface evaporation fractionation and lateral terrestrial water flow on $\delta_P{}^{18}$O, $\delta_P{}^{2}$H, and d_P at the selected stations. Figure 8 confirms the good correspondence between modeled and observed climatological monthly variations, at least for $\delta_P{}^{18}$O and $\delta_P{}^{2}$H in Europe, and displays small differences among simulation results. In Europe, $\delta_P{}^{18}$O and $\delta_P{}^{2}$H follow a seasonal cycle with a maximum reached during summer, which is a well-known temperature effect (e.g., Dansgaard, 1964). In Southern Africa, the seasonal variations of $\delta_P{}^{18}$O and $\delta_P{}^{2}$H are much smaller with a maximum during winter, which is the opposite situation in comparison to Europe. Indeed, lower precipitation amounts during winter for the entire Southern Africa are associated with larger isotopic concentrations, and this amount effect (e.g., Dansgaard, 1964) appears to overbalance the temperature effect in this case. However, these isotopic variations in Southern Africa are not well captured in the model, with a large negative bias most of the year.

For both Europe and Southern Africa, the largest difference in simulation results for $\delta_P{}^{18}$O and $\delta_P{}^{2}$H occurs between sim1 and sim2, which represents the effect of surface evaporation fractionation. This confirms the small but noticeable impact of surface evaporation fractionation on precipitation isotopic concentrations, as discussed by Christner et al. (2018) for summer precipitation in Europe, and by Risi et al. (2016) at a global scale. Remarkably, for both Europe and Southern Africa, the consideration of surface evaporation fractionation slightly worsens the negative biases of $\delta_P{}^{18}$O and $\delta_P{}^{2}$H to observation. Reciprocally, Risi et al. (2016) found that this decreasing effect of surface evaporation fractionation on precipitation isotopic concentrations ameliorated their positive model biases to observations, especially in boreal continental regions.

In the case of d_P, the discrepancies between simulation results and observations are much larger, especially with respect to the seasonal cycle, as shown in Figures 8c and 8f. The lack of ability to simulate d_P was also reported with other models (e.g., Brady et al., 2019; Risi et al., 2016). Still, it is found that the consideration of surface evaporation fractionation mostly increases d_P as expected (e.g., Risi et al., 2016).

Quantitatively, in the case of Europe, the station-average GNIP mean values of ($\delta_P{}^{18}$O, $\delta_P{}^{2}$H, and d_P) are (−8.1‰, −55.9‰, and 9.1‰). These values are underestimated by (−0.2‰, −2.4‰, and −0.6‰) with sim1 and by (−0.4‰, −4.1‰, and −0.4‰) with either sim2 or sim3. The underestimation of $\delta_P{}^{18}$O and $\delta_P{}^{2}$H mainly occurs from late autumn to spring, as can be seen in Figures 8a and 8b, and could be caused by the cold temperature bias discussed above. The negative biases in precipitation isotopic concentrations may also partly originate from the isotopic lateral boundary condition from the iCESM1/ERA5 forcing data set, as iCESM1 outputs display such negative biases as well (e.g., Brady et al., 2019).

In the case of Southern Africa, the station-average GNIP mean values of ($\delta_P{}^{18}$O, $\delta_P{}^{2}$H, and d_P) are (−4.0‰, −18.4‰, and 13.4‰), the higher values of $\delta_P{}^{18}$O and $\delta_P{}^{2}$H in comparison to Europe being related to the well-known temperature effect (e.g., Dansgaard, 1964). The higher value of d_P in comparison to Europe may indicate a more pronounced kinetic effect with land surface evaporation fractionation in Southern Africa. These values are underestimated/overestimated by (−1.0‰, −7.1‰, and 0.7‰) with sim1, by (−1.2‰, −8.0‰, and 1.6‰) with sim2, and by (−1.1‰, −7.4‰, and 1.7‰) with sim3. In comparison to global modeling literature results, Nusbaumer et al. (2017) and Brady et al. (2019) also found negative biases for $\delta_P{}^{18}$O and $\delta_P{}^{2}$H at Southern African GNIP stations, although a better matching was apparently met in Haese et al. (2013) and Risi et al. (2010).

The negative biases in precipitation isotopic concentrations may indicate that the rain droplet evaporation fractionation calculation from Nusbaumer et al. (2017), which is used here (see Section 2.8), overestimates the fraction of the rain water, which evaporates without fractionation, leading to more isotopically depleted precipitation at the ground especially during the cold season.

5.2. Comparison to Observation—Multi-Year Averaged Maps

The model skill in reproducing the climatological precipitation isotopic concentrations $\delta_P{}^{18}$O and $\delta_P{}^{2}$H and deuterium excess d_P from the GNIP data set is further evaluated with multi-year averaged maps in Figure 9. This figure shows that the spatial characteristics of precipitation isotopic concentrations, as deduced from the GNIP stations, are generally well captured by WRF-Hydro-iso.

In the case of Europe in Figures 9a and 9b, there is a well-defined altitude effect (e.g., Dansgaard, 1964), that is, a decrease in $\delta_P{}^{18}$O and $\delta_P{}^{2}$H with elevation, as well as a well-defined continental effect (e.g.,

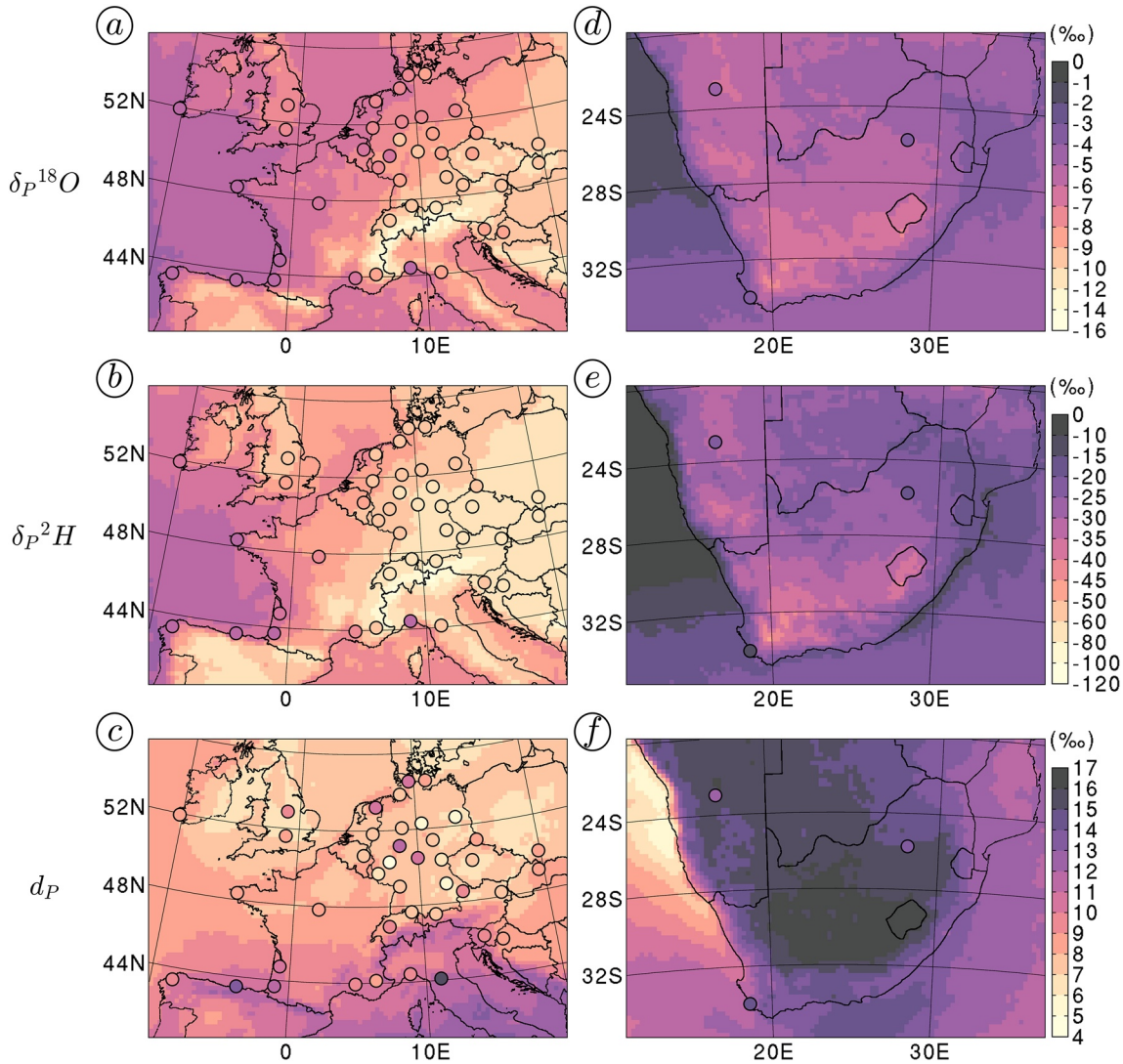

Figure 9. (a–c) Maps for Europe of modeled precipitation isotopic concentrations $\delta_P{}^{18}$O and $\delta_P{}^{2}$H and deuterium excess d_P for the period from 2003 to 2012, derived from sim1 and given in ‰. The circles indicate multi-year averaged observations at GNIP stations. (d–f) As in (a–c), except for Southern Africa.

Dansgaard, 1964), that is, a decrease in $\delta_P{}^{18}$O and $\delta_P{}^{2}$H from the Atlantic coast toward the east. These well-known altitude and continental effects are less clear in Figures 9d and 9e for Southern Africa. Indeed, Southern Africa is characterized by a high precipitation seasonality with a summer rainfall zone in the central and eastern regions and a winter rainfall zone near the west coast (e.g., Roffe et al., 2019), which also contributes to regional differences in isotopic concentrations (e.g., Herrmann et al., 2017). But the scarcity of the GNIP stations in Southern Africa does not allow to fully validate the modeled spatial distribution of isotopic concentrations in this case.

The deuterium excess d_P in Figures 9c and 9f reveals different spatial patterns in comparison to $\delta_P{}^{18}$O and $\delta_P{}^{2}$H, which may be the effect of relative humidity (Pfahl & Sodemann, 2014). However, the simulated spatial patterns of d_P do not match well with the GNIP observations, as also reported in literature (e.g., Brady et al., 2019).

Overall, the discrepancies between observed and modeled precipitation isotopic concentrations in Figures 8 and 9 are reasonably small, except for deuterium excess and comparable to what can be obtained with other regional models of water isotopologues (e.g., Christner et al., 2018). A detailed analysis of the impact of

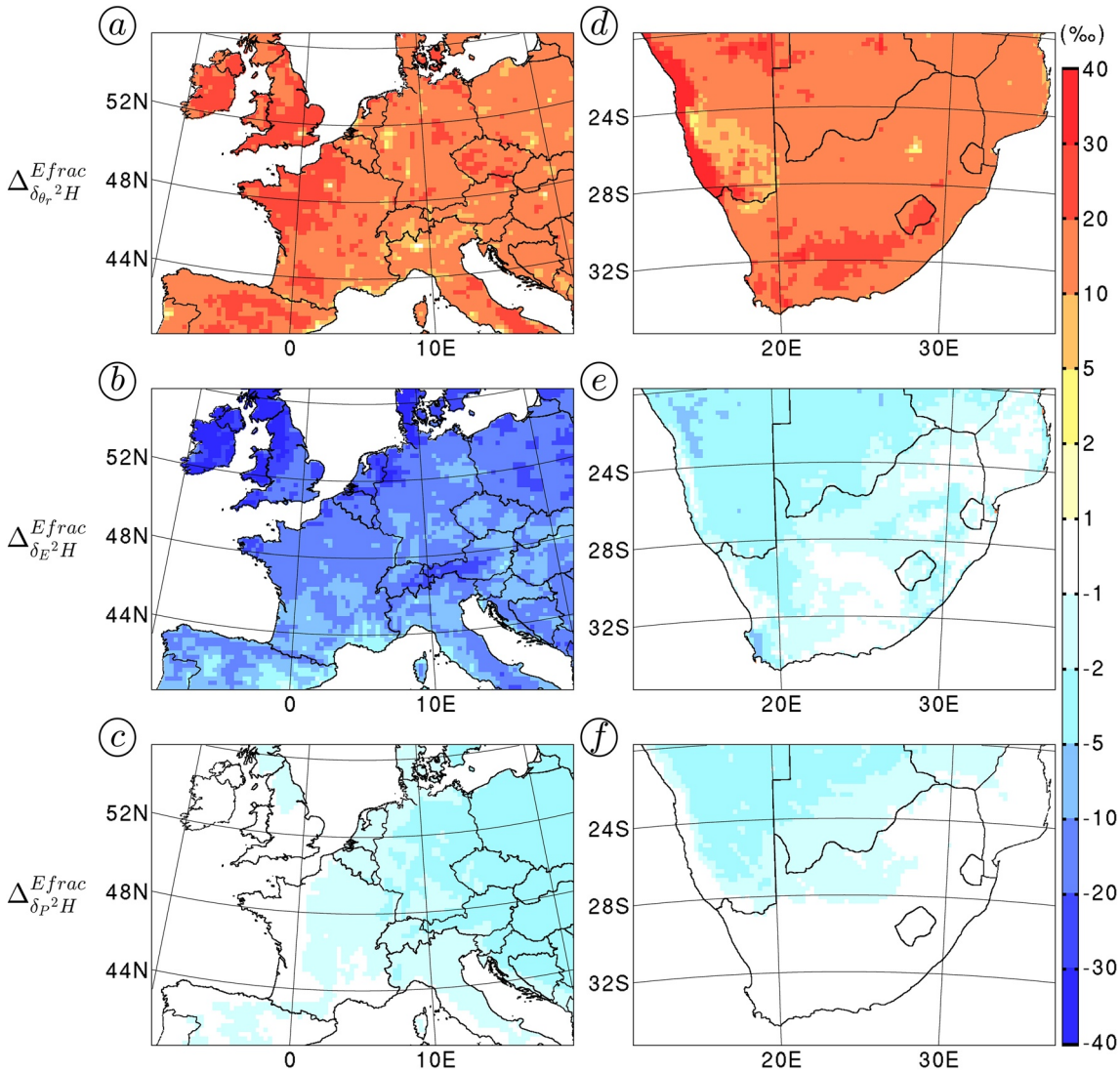

Figure 10. (a–c) Maps for Europe of the differences in modeled isotopic concentration introduced by the consideration of land surface evaporation fractionation in the rootzone soil moisture, surface evaporation, and precipitation for the case of δ^2H, namely $\Delta^{Efrac}_{\delta_{\theta_r}{}^2H}$, $\Delta^{Efrac}_{\delta_E{}^2H}$, and $\Delta^{Efrac}_{\delta_P{}^2H}$. These differences are computed according to Equation 12 for averaged water quantities over the period from 2003 to 2012 and are given in ‰. (d–f) As in (a–c), except for Southern Africa.

land surface evaporation fractionation and lateral terrestrial water on these spatial variabilities of isotopic concentrations is provided in the following subsections for the case of δ^2H.

5.3. Role of Land Surface Evaporation Fractionation

The role of land surface evaporation fractionation on isotopic concentrations is evaluated with multi-year averaged maps of $\Delta^{Efrac}_{\delta_{\theta_r}{}^2H}$, $\Delta^{Efrac}_{\delta_E{}^2H}$, and $\Delta^{Efrac}_{\delta_P{}^2H}$ in Figure 10, these Δ^{Efrac} differences being computed as in Equation 12.

The consideration of surface evaporation fractionation generally increases the rootzone soil moisture isotopic concentration $\delta_{\theta_r}{}^2$H and decreases the land surface evaporation isotopic concentration $\delta_E{}^2$H, as displayed in Figures 10a–10d and 10e with positive values of $\Delta^{Efrac}_{\delta_{\theta_r}{}^2H}$ and negative values of $\Delta^{Efrac}_{\delta_E{}^2H}$. The fact that the isotopic depletion of evaporation is less efficient for warmer temperatures (e.g., Majoube, 1971a, 1971b;

Merlivat & Nief, 1967) contributes to a smaller increase in $\delta_{\theta_r}{}^2\mathrm{H}$ and a smaller decrease in $\delta_E{}^2\mathrm{H}$ in Southern Africa.

For the particular case of $\delta_{\theta_r}{}^2\mathrm{H}$ in Southern Africa, the warm temperature effect is counterbalanced by a low soil moisture amount effect, as the rootzone soil moisture isotopic enrichment through land surface evaporation fractionation is quicker for lower soil moisture amounts. As a result, the multi-year averaged values of $\Delta^{\mathrm{Efrac}}_{\delta_{\theta_r}{}^2\mathrm{H}}$ in Figures 10a and 10d are comparable. Additionally, the decrease in $\delta_E{}^2\mathrm{H}$ in Southern Africa is reduced by the enhanced contribution of transpiration, which does not fractionate but instead experiences an isotopic concentration increase due to the increase in $\delta_{\theta_r}{}^2\mathrm{H}$.

For both Europe and Southern Africa, the decrease in $\delta_E{}^2\mathrm{H}$ shown in Figures 10b and 10e generally leads to a decrease in precipitation isotopic concentration $\delta_P{}^2\mathrm{H}$, as can be seen in Figures 10c and 10f with the negative values of $\Delta^{\mathrm{Efrac}}_{\delta_P{}^2\mathrm{H}}$, which is in agreement with the station-based results shown in Figure 9 and previously discussed at Section 5.1. In a sensitivity analysis conducted at a global scale, Haese et al. (2013) also found that the consideration of land surface evaporation fractionation mainly modifies the isotopic concentrations in soil moisture, and to a much smaller extent the isotopic concentrations in precipitation as well.

According to Figures 10c and 10f, the decrease in $\delta_P{}^2\mathrm{H}$ caused by land surface evaporation fractionation is generally enhanced downwind of the summer precipitation's region, that is, toward the East in Europe and toward the West in Southern Africa. Indeed, land precipitation recycling increases while atmospheric air masses travel through the land (e.g., Risi et al., 2013), leading to an increased contribution of $\delta_E{}^2\mathrm{H}$ to $\delta_P{}^2\mathrm{H}$ and a larger decrease in $\delta_P{}^2\mathrm{H}$ at the inland locations farthest from oceanic water sources. The fact that comparable values of $\Delta^{Efrac}_{\delta_P{}^2\mathrm{H}}$ are obtained in both regions, although Southern Africa experiences a much smaller decrease in $\delta_E{}^2\mathrm{H}$, suggest that the change in $\delta_P{}^2\mathrm{H}$ is more sensitive to the component of E characterized by lower isotopic concentrations, that is, the fractionating surface evaporation E_{ev}. This result corroborates previous findings that precipitation recycles more evaporation than transpiration (e.g., van der Ent et al., 2014; Wei et al., 2015).

5.4. Role of Lateral Terrestrial Water Flow

The role of lateral terrestrial water flow on isotopic concentrations is evaluated with multi-year averaged maps of $\Delta^{\mathrm{Hydro}}_{\delta_{\theta_r}{}^2\mathrm{H}}$, $\Delta^{\mathrm{Hydro}}_{\delta_E{}^2\mathrm{H}}$, and $\Delta^{\mathrm{Hydro}}_{\delta_P{}^2\mathrm{H}}$ in Figure 11, these Δ^{Hydro} differences being computed as in Equation 13.

For Europe, as detailed in Section 4.4, the consideration of lateral terrestrial water flow largely increases E_{ev} in most areas and sparsely increases E_{tr}, in association with a slight enhancement in precipitation. The increase in E_{ev} enhances the isotopic enrichment of the rootzone soil moisture through land surface evaporation fractionation, leading to the positive values of $\Delta^{\mathrm{Hydro}}_{\delta_{\theta_r}{}^2\mathrm{H}}$ in Figure 11a. The increase in E_{ev} also tends to reduce the land surface evaporation isotopic concentrations, although this effect is counterbalanced in the areas where the enhanced nonfractionating E_{tr} increases the transfer of isotopically enriched water from the rootzone toward the atmosphere, as displayed in Figure 11b. Overall, the changes in $\delta_P{}^2\mathrm{H}$ resulting from the consideration of lateral terrestrial water flow in Europe are very small, with values of $\Delta^{\mathrm{Hydro}}_{\delta_P{}^2\mathrm{H}}$ generally below 1‰ in Figure 11c.

In Southern Africa, as detailed in Section 4.4, the consideration of lateral terrestrial water flow largely increases E_{tr} and to a lesser extent also increases E_{ev} near the East coast, in association with a precipitation enhancement. In comparison to Europe, the increase in $\delta_{\theta_r}{}^2\mathrm{H}$ through land surface evaporation fractionation is weaker as shown by less positive values of $\Delta^{\mathrm{Hydro}}_{\delta_{\theta_r}{}^2\mathrm{H}}$ in Figure 11d, and the increase in $\delta_E{}^2\mathrm{H}$ through nonfractionating transpiration is stronger as shown by more positive values of $\Delta^{\mathrm{Hydro}}_{\delta_E{}^2\mathrm{H}}$ in Figure 11e. Overall, the changes in $\delta_P{}^2\mathrm{H}$ resulting from the consideration of lateral terrestrial water flow in Southern Africa is not as small as in Europe, with values of $\Delta^{\mathrm{Hydro}}_{\delta_P{}^2\mathrm{H}}$ reaching 2‰ near the eastern coastal region in Figure 11f.

For both Europe and Southern Africa, the effect of lateral terrestrial water flow on isotopic concentrations remains minor in comparison to the effect of land surface evaporation fractionation detailed in previous

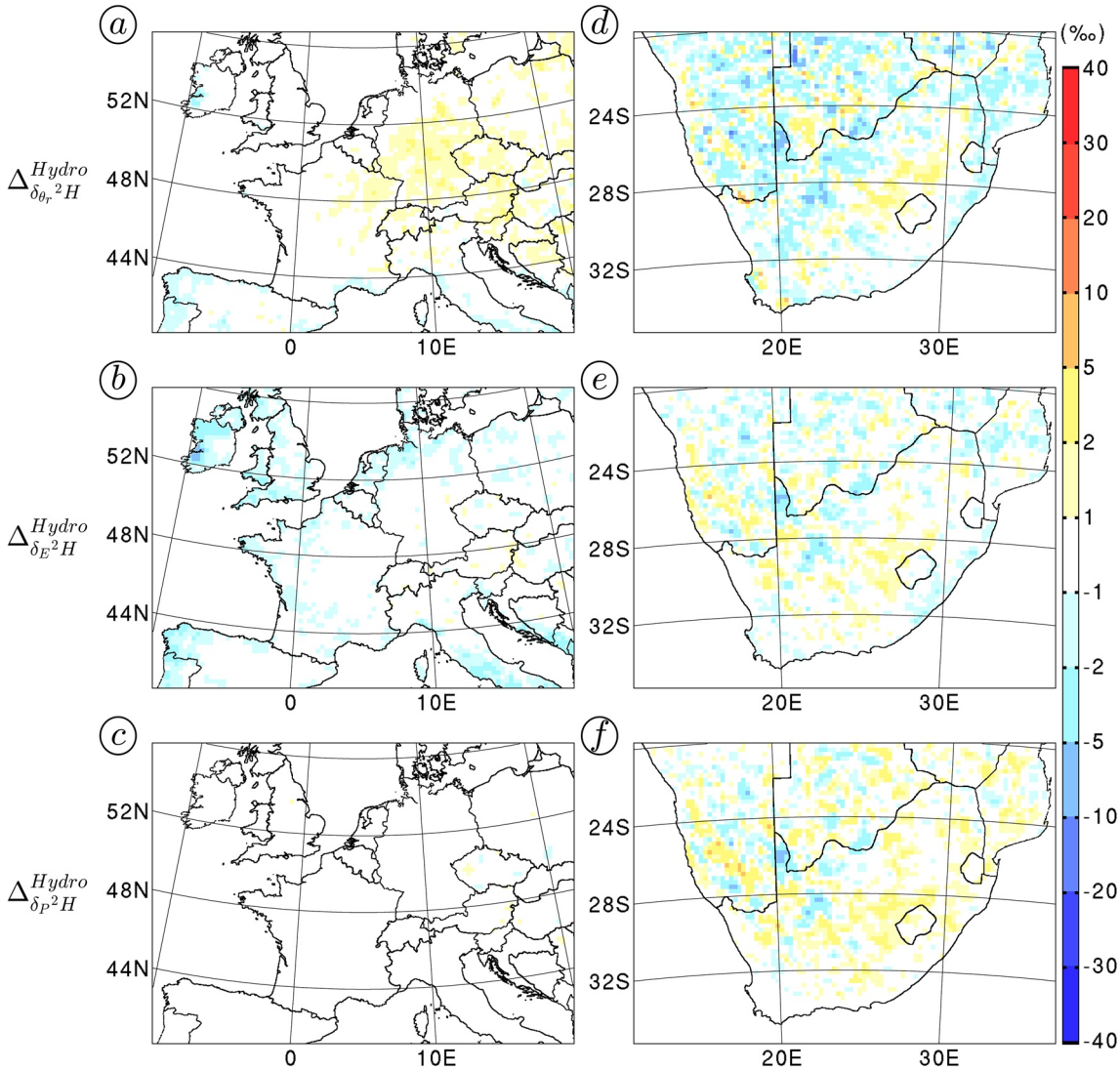

Figure 11. (a–c) Maps for Europe of the differences in modeled isotopic concentration introduced by the consideration of lateral terrestrial water flow in the rootzone soil moisture, surface evaporation, and precipitation for the case of δ^2H, namely $\Delta^{\text{Hydro}}_{\delta_{\theta_r}{}^2\text{H}}$, $\Delta^{\text{Hydro}}_{\delta_E{}^2\text{H}}$, and $\Delta^{\text{Hydro}}_{\delta_P{}^2\text{H}}$. These differences are computed according to Equation 13 for averaged water quantities over the period from 2003 to 2012 and are given in ‰. (d–f) As in (a–c), except for Southern Africa.

section. Indeed, we find that it is the ratio between transpiration and direct evaporation, which matters for isotopic concentrations in the rootzone, and the lateral terrestrial water flow only induces minor changes to this ratio.

The scatteredness of positive and negative values of $\Delta^{\text{Hydro}}_{\delta_{\theta_r}{}^2\text{H}}$, $\Delta^{\text{Hydro}}_{\delta_E{}^2\text{H}}$, and $\Delta^{\text{Hydro}}_{\delta_P{}^2\text{H}}$ in Figures 11d–11f, respectively, may be related to random fluctuations in the modeled relationship between transpiration, precipitation, and soil moisture, which are not fully smoothed in the 10-year mean simulations' results. Nevertheless, the general increase in $\delta_P{}^2$H is attributed to the increase in nonfractionating transpiration, which brings more isotopically enriched water in the atmosphere to be recycled as precipitation. Accordingly, specifically in the case of Southern Africa, the consideration of lateral terrestrial water flow increases the contribution of transpiration to precipitation (e.g., Wei et al., 2015).

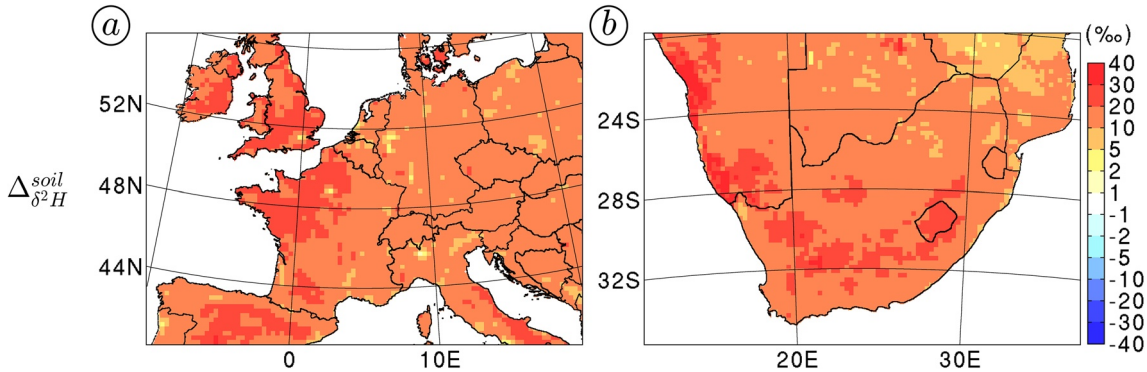

Figure 12. (a) Map for Europe of the difference in modeled isotopic concentration between precipitation and the rootzone soil moisture for the case of δ^2H, namely $\Delta^{soil}_{\delta^2 H}$. $\Delta^{soil}_{\delta^2 \mathrm{H}}$ is computed according to Equation 14 for averaged water quantities over the period from 2003 to 2012 and is given in ‰. (b) As in (a), except for Southern Africa.

5.5. Difference Between Rootzone and Precipitation Isotopic Concentrations

The difference in isotopic concentrations between precipitation and rootzone soil moisture is evaluated with multi-year averaged maps of $\Delta^{\mathrm{soil}}_{\delta^2 \mathrm{H}}$ in Figure 12, computed as in Equation 14. For both Europe and Southern Africa, Figure 12 displays much positive values of $\Delta^{\mathrm{soil}}_{\delta^2 \mathrm{H}}$. Quantitatively, Figure 12 indicates that $\delta_{\theta_r}{}^2\mathrm{H}$ is generally 10–20‰ above $\delta_P{}^2\mathrm{H}$, which is mainly due to the land surface evaporation fractionation discussed above in Section 5.3. Lateral terrestrial water flow may slightly enhance this land surface fractionation effect in relatively wet regions like Europe, due to the preference of lateral terrestrial water flow to increase direct evaporation rather than transpiration for wet soils. The knowledge of such processes affecting $\delta_{\theta_r}{}^2\mathrm{H}$ is certainly important for a quantitative paleo-precipitation reconstruction from organic sediments having transited through the rootzone, such as plant leaf waxes.

6. Summary and Perspectives

This study presents the newly developed WRF-Hydro-iso, which is a version of the coupled atmospheric-hydrological modeling system WRF-Hydro from Gochis et al. (2018) enhanced with a joint description of soil-vegetation-atmospheric water isotopologues motions. WRF-Hydro-iso has been applied to two present-climate cases, one in Europe and the other in Southern Africa. The boundary condition of the usual land-atmospheric variables in WRF-Hydro-iso has been taken from the ERA5 reanalyses, whereas the boundary condition of the isotopic variables has been deduced from climatological values derived from a 10-year iCESM1 simulation. In both cases, the WRF-Hydro-iso model driven with this hybrid ERA5/iCESM1 data set proved abilities in reproducing present-day climatological precipitation isotopic concentrations $\delta_P{}^{18}\mathrm{O}$ and $\delta_P{}^2\mathrm{H}$ from GNIP. The model bias to isotopic observations was larger in Southern Africa, which shows that the model can still be improved for specific regions. Nevertheless, a sensitivity analysis was carried out to investigate the respective effect of land surface evaporation and lateral terrestrial water flow on the simulated isotopic concentrations with WRF-Hydro-iso, with the objective to evaluate the potential benefit of using a coupled atmospheric-hydrological model for water isotopologue modeling.

The consideration of land surface evaporation fractionation strongly increased the isotopic concentrations in the rootzone soil moisture and slightly decreased the isotopic concentrations in precipitation, in agreement with a previous study from Haese et al. (2013). In comparison, the consideration of lateral terrestrial water flow had a much lower impact on the isotopic concentrations in the rootzone soil moisture. Still, lateral terrestrial water flow clearly increased the land surface evaporation. In relatively wetter Europe, the increase in land surface evaporation mostly concerned the *fractionating* direct evaporation, so that in this case the lateral terrestrial water flow also enhanced the isotopic enrichment of the rootzone soil moisture through a larger land surface evaporation fractionation. In relatively drier Southern Africa, the increase in land surface evaporation concerned with a larger proportion of the nonfractionating transpiration, which

induced a larger transfer of isotopically enriched water from the rootzone toward the atmosphere that partly recycled as precipitation, thus slightly increased the precipitation isotopic concentrations.

This modest impact of lateral terrestrial water flow on isotopic concentrations indicates that this process is secondary for the interpretation of paleo records data. The effect of more dominant factors controlling the ratio between transpiration and direct evaporation, such as plant types (e.g., Hou et al., 2007), should be considered in a future sensitivity analysis. This is particularly relevant for the interpretation of paleo records associated with pronounced vegetation changes, such as in Southern Africa (e.g., Burdanowitz et al., 2018).

This first study with WRF-Hydro-iso shows the potential of this model for simulating isotopic concentrations in each compartment of the soil-vegetation-atmosphere system at regional scale. Future applications could focus on assessing the WRF-Hydro-iso performances with respect to other water isotopologue data sets, such as water vapor isotopic concentrations deduced from remote-sensing techniques (e.g., Christner et al., 2018; Risi et al., 2013) and soil moisture isotopic concentrations from in-situ measurements (e.g., Gazis & Feng, 2004; Risi et al., 2016; Wong et al., 2017). As a coupled atmospheric-hydrological modeling system, WRF-Hydro-iso theoretically offers the possibility to estimate isotopic concentrations in streamflow, which could provide an innovative approach in the field of transit time research (e.g., Kirchner, 2019). Finally, as a regional model, WRF-Hydro-iso can be applied to the dynamical downscaling of global paleoclimate simulations (Ludwig et al., 2019) in order to simulate isotopic concentrations in the rootzone, which can potentially enable a more direct comparison between model results and proxy data related to plants (e.g., Dupont et al., 2013), and might also alter the interpretation of paleoclimate proxy records.

Data Availability Statement

The WRF-Hydro-iso source code, which has been used in this study, together with a test application case can be downloaded at https://figshare.com/s/74257d1f6a508afa9334. The iCESM model is available at https://github.com/NCAR/iCESM1.2. The ERA5 data set has been generated using the Copernicus Climate Change Service Climate Data Store (CDS), https://cds.climate.copernicus.eu/cdsapp#!/home. HydroSHEDS data can be found at: https://www.hydrosheds.org/downloads, and the WRF-Hydro preprocessing tool at: https://ral.ucar.edu/projects/wrf_hydro/pre-processing-tools. The observational data sets used in this study are available online, the Global Network of Isotopes in Precipitation data set of the International Atomic Energy Agency and the World Meteorology Organization at https://nucleus.iaea.org/wiser/index.aspx, the precipitation and temperature data sets from the ECA&D project at http://www.ecad.eu, the precipitation data set from the Climate Hazard Center at https://www.chc.ucsb.edu/data/chirps/, and the temperature data set from the Climate Research Unit at http://www.cru.uea.ac.uk/cru/data/hrg/.

Acknowledgments
This research is funded by the German Science Foundation (DFG, grant AR 1183/2-1, grant KU 2090/11-1, AccHydro project), the German Federal Ministry of Science and Education (BMBF, SALDi project), and the Bavarian State Ministry of Science and the Arts (LANDKLIF project). The source code of iCESM1 was provided by Jesse Nusbaumer. The iCESM1 simulation that has been used to prescribe the boundary condition of isotopic variables in WRF-Hydro-iso was performed at the North-German Supercomputing Alliance HLRN and the Center for Marine Environmental Sciences (MARUM), Bremen. Model developments and simulations with WRF-Hydro-iso were performed on the computational resource ForHLR II funded by the Ministry of Science, Research and the Arts Baden-Württemberg and DFG. Special thanks go to Paul André for sharing isotope modeling tips, David Martin Belda for a fruitful discussion about land surface evaporation, and Christoph Sörgel, Peter Weisbrod, Roland Laifer, and Hartmut Häfner for their computer support. Open access funding enabled and organized by Projekt DEAL.

References

Aemisegger, F., Pfahl, S., Sodemann, H., Lehner, I., Seneviratne, S. I., & Wernli, H. (2014). Deuterium excess as a proxy for continental moisture recycling and plant transpiration. *Atmospheric Chemistry and Physics*, *14*, 4029–4054. https://doi.org/10.5194/acp-14-4029-2014

Aemisegger, F., Spiegel, J. K., Pfahl, S., Sodemann, H., Eugster, W., & Wernli, H. (2015). Isotope meteorology of cold front passages: A case study combining observations and modeling. *Geophysical Research Letters*, *42*, 5652–5660. https://doi.org/10.1002/2015GL063988

Anyah, R. O., Weaver, C. P., Miguez-Macho, G., Fan, Y., & Robock, A. (2008). Incorporating water table dynamics in climate modeling: 3. Simulated groundwater influence on coupled land–atmosphere variability. *Journal of Geophysical Research*, *113*, D0703. https://doi.org/10.1029/2007JD009087

Arnault, J., Fersch, B., Rummler, T., Zhang, Z., Quenum, G. M., Wei, J., et al. (2021). Lateral terrestrial water flow contribution to summer precipitation at continental scale—A comparison between Europe and West Africa with WRF-Hydro-tag ensembles. *Hydrological Processes*, *35*, e14183. https://doi.org/10.1002/hyp.14183

Arnault, J., Knoche, R., Wei, J., & Kunstmann, H. (2016). Evaporation tagging and atmospheric water budget analysis with WRF: A regional precipitation recycling study for West Africa. *Water Resources Research*, *52*, 1544–1567. https://doi.org/10.1002/2015WR017704

Arnault, J., Rummler, T., Baur, F., Lerch, S., Wagner, S., & Fersch, B., et al. (2018). Precipitation sensitivity to the uncertainty of terrestrial water flow in WRF-Hydro: An ensemble analysis for Central Europe. *Journal of Hydrometeorology*, *19*, 1007–1025. https://doi.org/10.1175/JHM-D-17-0042.1

Arnault, J., Wagner, S., Rummler, T., Fersch, B., Bliefernicht, J., Andresen, S., & Kunstmann, H. (2016). Role of runoff–infiltration partitioning and resolved overland flow on land–atmosphere feedbacks: A case study with the WRF-Hydro coupled modeling system for West Africa. *Journal of Hydrometeorology*, *17*, 1489–1516. https://doi.org/10.1175/jhm-d-15-0089.1

Arnault, J., Wei, J., Rummler, T., Fersch, B., Zhang, Z., Jung, G., et al. (2019). A joint soil-vegetation-atmospheric water tagging procedure with WRF-Hydro: Implementation and application to the case of precipitation partitioning in the upper Danube river basin. *Water Resources Research*, *55*, 6217–6243. https://doi.org/10.1029/2019WR024780

Blossey, P. N., Kuang, Z., & Romps, D. M. (2010). Isotopic composition of water in the tropical tropopause layer in cloud-resolving simulations of an idealized tropical circulation. *Journal of Geophysical Research*, *115*, D24309. https://doi.org/10.1029/2010JD014554

Blumthaler, M., Ambach, W., & Ellinger, R. (1997). Increase in solar UV radiation with altitude. *Journal of Photochemistry and Photobiology B: Biology*, *39*, 130–134. https://doi.org/10.1016/s1011-1344(96)00018-8

Brady, E., Stevenson, S., Bailey, D., Liu, Z., Noone, D., Nusbaumer, J., et al. (2019). The connected isotopic water cycle in the Community Earth System Model version 1. *Journal of Advances in Modeling Earth Systems*, *11*, 2547–2566. https://doi.org/10.1029/2019MS001663

Burdanowitz, N., Dupont, L., Zabel, M., & Schefuß, E. (2018). Holocene hydrologic and vegetation developments in the Orange River catchment (South Africa) and their controls. *The Holocene*, *28*, 1288–1300. https://doi.org/10.1177/0959683618771484

Christner, E., Aemisegger, F., Pfahl, S., Werner, M., Cauquoin, A., Schneider, M., et al. (2018). The climatological impacts of continental surface evaporation, rainout, and subcloud processes on δD of water vapor and precipitation in Europe. *Journal of Geophysical Research: Atmospheres*, *123*, 4390–4409. https://doi.org/10.1002/2017JD027260

Craig, H. (1961). Isotopic variations in meteoric waters. *Science*, *133*, 1702–1703. https://doi.org/10.1126/science.133.3465.1702

Crétat, J., Pohl, B., Richard, Y., & Drobinski, P. (2012). Uncertainties in simulating regional climate of Southern Africa: Sensitivity to physical parameterizations using WRF. *Climate Dynamics*, *38*, 613–634. https://doi.org/10.1007/s00382-011-1055-8

Dansgaard, W. (1954). The O^{18}-Abundance in fresh water. *Geochimica et Cosmochimica Acta*, *6*, 241–260. https://doi.org/10.1016/0016-7037(54)90003-4

Dansgaard, W. (1964). Stable isotopes in Precipitation. *Tellus*, *16*, 436–468. https://doi.org/10.1111/j.2153-3490.1964.tb00181.x

Dansgaard, W., Johnsen, S. J., Moller, J., & Langway, C. C. (1969). One thousand centuries of climatic record from camp century on the Greenland ice sheet. *Science*, *166*, 377–380. https://doi.org/10.1126/science.166.3903.377

Dirmeyer, P. A., Cash, B. A., Kinter, J. L., Stan, C., Jung, T., Marx, L., et al. (2012). Evidence for enhanced land–atmosphere feedback in a warming climate. *Journal of Hydrometeorology*, *13*, 981–995. https://doi.org/10.1175/jhm-d-11-0104.1

Dudhia, J. (1989). Numerical study of convection observed during the Winter Monsoon Experiment using a mesoscale two-dimensional model. *Journal of the Atmospheric Sciences*, *46*, 3077–3107. https://doi.org/10.1175/1520-0469(1989)046<3077:nsocod>2.0.co;2

Dupont, L. M., Rommerskirchen, F., Mollenhauer, G., & Schefuß, E. (2013). Miocene to Pliocene changes in South African hydrology and vegetation in relation to the expansion of C4 plants. *Earth and Planetary Science Letters*, *375*, 408–417. https://doi.org/10.1016/j.epsl.2013.06.005

Eckstein, J., Ruhnke, R., Pfahl, S., Christner, E., Diekmann, C., Dyroff, C., et al. (2018). From climatological to small-scale applications: Simulating water isotopologues with ICON-ART-Iso (version 2.3). *Geoscientific Model Development*, *11*, 5113–5133. https://doi.org/10.5194/gmd-11-5113-2018

Fersch, B., Senatore, A., Adler, B., Arnault, J., Mauder, M., Schneider, K., et al. (2020). High-resolution fully-coupled atmospheric–hydrological modeling: A cross-compartment regional water and energy cycle evaluation. *Hydrology and Earth System Sciences*, *24*, 2457–2481. https://doi.org/10.5194/hess-24-2457-2020

Field, R. D., Jones, D. B. A., & Brown, D. P. (2010). Effects of postcondensation exchange on the isotopic composition of water in the atmosphere. *Journal of Geophysical Research*, *115*, D24305. https://doi.org/10.1029/2010JD014334

Friedl, M. A., McIver, D. K., Hodges, J. C. F., Zhang, X. Y., Muchoney, D., Strahler, A. H., et al. (2002). Global land cover mapping from MODIS: Algorithms and early results. *Remote Sensing of Environment*, *83*, 287–302. https://doi.org/10.1016/S0034-4257(02)00078-0

Friedman, I., Machta, L., & Soller, R. (1962). Water-vapor exchange between a water droplet and its environment. *Journal of Geophysical Research*, *67*, 2761–2766. https://doi.org/10.1029/JZ067i007p02761

Funk, C., Peterson, P., Landsfeld, M., Pedreros, D., Verdin, J., Shukla, S., et al. (2015). The climate hazards infrared precipitation with stations—A new environmental record for monitoring extremes. *Scientific Data*, *2*, 150066. https://doi.org/10.1038/sdata.2015.66

Gat, J. R. (1996). Oxygen and hydrogen isotopes in the hydrological cycle. *Annual Review of Earth and Planetary Sciences*, *24*, 225–262. https://doi.org/10.1146/annurev.earth.24.1.225

Gazis, C., & Feng, X. (2004). A stable isotope study of soil water: Evidence for mixing and preferential flow paths. *Geoderma*, *119*, 97–111. https://doi.org/10.1016/S0016-7061(03)00243-X

Gochis, D. J., Barlage, M., Dugger, A., FitzGerald, K., Karsten, L., McAllister, M., et al. (2018). *The WRF-Hydro modeling system technical description (version 5.0)* (NCAR Technical Note, p. 107). Retrieved from https://ral.ucar.edu/projects/wrf_hydro/technical-description-user-guide

Haese, B., Werner, M., & Lohmann, G. (2013). Stable water isotopes in the coupled atmosphere-land surface model ECHAM5-JSBACH. *Geoscientific Model Development*, *6*, 1463–1480. https://doi.org/10.5194/gmd-6-1463-2013

Haiden, T., Balsamo, G., Sandu, I., & Arduini, G. (2018). Addressing biases in near-surface forecasts. *ECMWF Newsletter*, *157*, 20–25. https://doi.org/10.21957/eng71d53th

Harris, I., Jones, P. D., Osborn, T. J. & Lister, D. H. (2014). Updated high-resolution grids of monthly climatic observations—The CRU TS3.10 dataset. *International Journal of Climatology*, *34*, 623–642. https://doi.org/10.1002/joc.3711

Haylock, M. R., Hofstra, N., Klein Tank, A. M. G., Klok, E. J., Jones, P. D., & New, M. (2008). A European daily high-resolution gridded dataset of surface temperature and precipitation. *Journal of Geophysical Research*, *113*, D20119. https://doi.org/10.1029/2008JD010201

Herrmann, N., Boom, A., Carr, A., Chase, B., Zabel, M., & Schefuß, E. (2017). Hydrogen isotopic fractionation of leaf-wax n-alkanes in southern African soils. *Organic Geochemistry*, *109*, 1–13. https://doi.org/10.1016/j.orggeochem.2017.03.008

Hersbach, H., Bell, B., Berrisford, P., Hirahara, S., Horányi, A., Muñoz-Sabater, J., et al. (2020). The ERA5 global reanalysis. *Quarterly Journal of Royal Meteorological Society*, *146*, 1999–2049. https://doi.org/10.1002/qj.3803

Hoffmann, G., Werner, M., & Heimann, M. (1998). Water isotope module of the ECHAM atmospheric general circulation model: A study on timescales from days to several years. *Journal of Geophysical Research*, *103*, 871–896. https://doi.org/10.1029/98JD00423

Hong, S.-Y., & Lim, J.-O. J. (2006). The WRF single-moment 6-class microphysics scheme (WSM6). *Journal of the Korean Meteorological Society*, *42*, 129–151.

Hou, J., D'Andrea, W. J., MacDonald, D., & Huang, Y. (2007). Hydrogen isotopic variability in leaf waxes among terrestrial and aquatic plants around Blood Pond, Massachusetts (USA). *Organic Geogemistry*, *38*, 977–984. https://doi.org/10.1016/j.orggeochem.2006.12.009

IAEA/WMO. (2020). *Global network of isotopes in precipitation* (The GNIP database). Retrieved from https://nucleus.iaea.org/wiser

Jacob, H., & Sonntag, C. (1991). An 8-year record of the seasonal variation of ^{2}H and ^{18}O in atmospheric water vapour and precipitation at Heidelberg, Germany. *Tellus B: Chemical and Physical Meteorology*, *43*, 291–300. https://doi.org/10.1034/j.1600-0889.1991.t01-2-00003.x

Joussaume, S., Sadourny, R., & Jouzel, J. (1984). A general circulation model of water isotope cycles in the atmosphere. *Nature*, *311*, 24–29. https://doi.org/10.1038/311024a0

Jouzel, J., & Merlivat, L. (1984). Deuterium and oxygen 18 in precipitation: Modeling of the isotopic effects during snow formation. *Journal of Geophysical Research*, *89*, 11749–11757. https://doi.org/10.1029/JD089iD07p11749

Jung, M., Reichstein, M., & Bondeau, A. (2009). Towards global empirical upscaling of FLUXNET eddy covariance observations: Validation of a model tree ensemble approach using a biosphere model. *Biogeosciences*, *6*, 2001–2013. https://doi.org/10.5194/bg-6-2001-2009

Jung, M., Reichstein, M., Ciais, P., Seneviratne, S. I., Sheeld, J., Goulden, M. L., et al. (2010). Recent decline in the global land evapotranspiration trend due to limited moisture supply. *Nature*, *467*, 951–954. https://doi.org/10.1038/nature09396

Kalognomou, E.-A., Lennard, C., Shongwe, M., Pinto, I., Favre, A., Kent, M., et al. (2013). A diagnostic evaluation of precipitation in CORDEX models over Southern Africa. *Journal of Climate*, *26*, 9477–9506. https://doi.org/10.1175/JCLI-D-12-00703.1

Kirchner, J. W. (2019). Quantifying new water fractions and transit time distributions using ensemble hydrograph separation: Theory and benchmark tests. *Hydrology and Earth System Sciences*, *23*, 303–349. https://doi.org/10.5194/hess-23-303-2019

Konecky, B. L., McKay, N. P., Churakova (Sidorova), O. V., Comas-Bru, L., Dassié, E. P., DeLong, K. L., et al. (2020). The Iso2k database: A global compilation of paleo-$\delta^{18}O$ and $\delta^{2}H$ records to aid understanding of Common Era climate. *Earth System Science Data*, *12*, 2261–2288. https://doi.org/10.5194/essd-12-2261-2020

Larsen, M. A. D., Christensen, J. H., Drews, M., Butts, M. B., & Refsgaard, J. C. (2016). Local control on precipitation in a fully coupled climate-hydrology model. *Scientific Reports*, *6*, 22927. https://doi.org/10.1038/srep22927

Lehner, B., Verdin, K., & Jarvis, A. (2008). New global hydrography derived from spaceborne elevation data. *Eos, Transactions, American Geophysical Union*, *89*(10), 93–94. https://doi.org/10.1029/2008EO100001

Ludwig, P., Gómez-Navarro, J. J., Pinto, J. G., Raible, C. C., Wagner, S., & Zorita, E. (2019). Perspectives of regional paleoclimate modeling. *Annals of the New York Academy of Sciences*, *1436*, 54–69. https://doi.org/10.1111/nyas.13865

Majoube, M. (1971a). Fractionnement en ^{18}O entre la glace et la vapeur d'eau. *Journal de Chime Physique*, *68*, 625–636. https://doi.org/10.1051/jcp/1971680625

Majoube, M. (1971b). Fractionnement en oxygene 18 et en deutérium entre l'eau et sa vapeur. *Journal de Chime Physique*, *68*, 1423–1436. https://doi.org/10.1051/jcp/1971681423

Maxwell, R. M., Lundquist, J. K., Mirocha, J. D., Smith, S. G., Woodward, C. S., & Tompson, A. F. (2011). Development of a coupled groundwater-atmosphere model. *Monthly Weather Review*, *139*, 96–116. https://doi.org/10.1175/2010MWR3392.1

Merlivat, L., & Jouzel, J. (1979). Global climatic interpretation of the deuterium-oxygen 18 relationship for precipitation. *Journal of Geophysical Research*, *84*, 5029–5033. https://doi.org/10.1029/JC084iC08p05029

Merlivat, L., & Nief, G. (1967). Fractionnement isotopique lors des changements d'état solide-vapeur et liquide-vapeur de l'eau à des températures inférieures à 0°C. *Tellus*, *19*, 122–127. https://doi.org/10.1111/j.2153-3490.1967.tb01465.x

Mlawer, E. J., Taubman, S. J., Brown, P. D., Iacono, M. J., & Clough, S. A. (1997). Radiative transfer for inhomogeneous atmosphere: RRTM, a validated correlated-k model for the long-wave. *Journal of Geophysical Research*, *102*, 16663–16682. https://doi.org/10.1029/97JD00237

Moore, M., Blossey, P. N., Muhlbauer, A., & Kuang, Z. (2016). Microphysical controls on the isotopic composition of wintertime orographic precipitation. *Journal of Geophysical Research: Atmosphere*, *121*, 7235–7253. https://doi.org/10.1002/2015JD023763

Niu, G.-Y., Yang, Z.-L., Mitchell, K. E., Chen, F., Ek, M. B., Barlage, M., et al. (2011). The community Noah land surface model with multiparameterization options (Noah-MP): 1. Model description and evaluation with local-scale measurements. *Journal of Geophysical Research*, *116*, D12109. https://doi.org/10.1029/2010JD015139

Nusbaumer, J., Wong, T. E., Bardeen, C., & Noone, D. (2017). Evaluating hydrological processes in the Community Atmosphere Model Version 5 (CAM5) using stable isotope ratios of water. *Journal of Advances in Modeling Earth Systems*, *9*, 949–977. https://doi.org/10.1002/2016MS000839

Pfahl, S., & Sodemann, H. (2014). What controls deuterium excess in global precipitation? *Climate of the Past*, *10*, 771–781. https://doi.org/10.5194/cp-10-771-2014

Pfahl, S., Wernli, H., & Yoshimura, K. (2012). The isotopic composition of precipitation from a winter storm—A case study with the limited-area model $COSMO_{iso}$. *Atmospheric Chemistry and Physics*, *12*, 1629–1648. https://doi.org/10.5194/acp-12-1629-2012

Pleim, J. E. (2007). A combined local and nonlocal closure model for the atmospheric boundary layer. Part I: Model description and testing. *Journal of Applied Meteorology and Climatology*, *46*, 1383–1395. https://doi.org/10.1175/JAM2539.1

Prein, A. F., Gobiet, A., TruhetzKeulerGoergen, H. K. K., Teichmann, C., Goergen, K., Teichmann, C., et al. (2016). Precipitation in the EURO-CORDEX 0.11° and 0.44° simulations: High resolution, high benefits? *Climate Dynamics*, *46*, 383–412. https://doi.org/10.1007/s00382-015-2589-y

Ratna, S. B., Ratnam, J. V., Behera, S. K., deW Rautenbach, C. J., Ndarana, T., Takahashi, K., & Yamagata, T. (2014). Performance assessment of three convective parameterization schemes in WRF for downscaling summer rainfall over South Africa. *Climate Dynamics*, *42*, 2931–2953. https://doi.org/10.1007/s00382-013-1918-2

Risi, C., Bony, S., & Vimeux, F. (2008). Influence of convective processes on the isotopic composition ($\delta^{18}O$ and δD) of precipitation and water vapor in the tropics: 2. Physical interpretation of the amount effect. *Journal of Geophysical Research*, *113*, D19306. https://doi.org/10.1029/2008JD009943

Risi, C., Bony, S., Vimeux, F., & Jouzel, J. (2010). Water-stable isotopes in the LMDZ4 general circulation model: Model evaluation for present-day and past climates and applications to climatic interpretations of tropical isotopic records. *Journal of Geophysical Research*, *115*, D12118. https://doi.org/10.1029/2009JD013255

Risi, C., Noone, D., Frankenberg, C., & Worden, J. (2013). Role of continental recycling in intraseasonal variations of continental moisture as deduced from model simulations and water vapor isotopic measurements. *Water Resources Research*, *49*, 4136–4156. https://doi.org/10.1002/wrcr.20312

Risi, C., Noone, D., Worden, J., Frankenberg, C., Stiller, G., Kiefer, M., et al. (2012). Process-evaluation of tropospheric humidity simulated by general circulation models using water vapor isotopic observations: 2. Using isotopic diagnostics to understand the mid and upper tropospheric moist bias in the tropics and subtropics. *Journal of Geophysical Research*, *117*, D05304. https://doi.org/10.1029/2011JD016623

Risi, C., Ogée, J., Bony, S., Bariac, T., Raz-Yaseef, N., Wingate, L., et al. (2016). The water isotopic version of the land-surface model ORCHIDEE: Implementation, evaluation, sensitivity to hydrological parameters. *Hydrology: Current Research*, *7*, 1–24. https://doi.org/10.4172/2157-7587.1000258

Roffe, S. J., Fitchett, J. M., & Curtis, C. J. (2019). Classifying and mapping rainfall seasonality in South Africa: A review. *South African Geographical Journal*, *101*, 158–174. https://doi.org/10.1080/03736245.2019.1573151

Rummler, T., Arnault, J., Gochis, D., & Kunstmann, H. (2019). Role of lateral terrestrial water flow on the regional water cycle in a complex terrain region: Investigation with a fully coupled model system. *Journal of Geophysical Research: Atmospheres*, *124*, 507–529. https://doi.org/10.1029/2018JD029004

Schefuß, E., Kuhlmann, H., Mollenhauer, G., Prange, M., & Pätzold, J. (2011). Forcing of wet phases in southeast Africa over the past 17,000 years. *Nature*, *480*, 509–512. https://doi.org/10.1038/nature10685

Skamarock, W. C., & Klemp, J. B. (2008). A time-split nonhydrostatic atmospheric model for weather research and forecasting applications. *Journal of Computational Physics*, *227*, 3465–3485. https://doi.org/10.1016/j.jcp.2007.01.037

Steen-Larsen, H. C., Risi, C., Werner, M., Yoshimura, K., & Masson-Delmotte, V. (2017). Evaluating the skills of isotope-enabled general circulation models against in situ atmospheric water vapor isotope observations. *Journal of Geophysical Research: Atmospheres*, *122*, 246–263. https://doi.org/10.1002/2016JD025443

Steppeler, J., Doms, G., Schättler, U., Bitzer, H. W., Gassmann, A., Damrath, U., & Gregoric, G. (2003). Meso-gamma scale forecasts using the nonhydrostatic model LM. *Meteorology and Atmospheric Physics*, *82*, 75–96. https://doi.org/10.1007/s00703-001-0592-9

Sulis, M., Keune, J., Shrestha, P., Simmer, C., & Kollet, S. J. (2018). Quantifying the impact of subsurface-land surface physical processes on the predictive skill of subseasonal mesoscale atmospheric simulations. *Journal of Geophysical Research: Atmospheres*, *123*, 9131–9151. https://doi.org/10.1029/2017JD028187

van der Ent, R. J., Wang-Erlandsson, L., Keys, P. W., & Savenije, H. H. G. (2014). Contrasting roles of interception and transpiration in the hydrological cycle—Part 2: Moisture recycling. *Earth System Dynamics*, *5*, 471–489. https://doi.org/10.5194/esd-5-471-2014

Wagner, S., Fersch, B., Yuan, F., Yu, Z., & Kunstmann, H. (2016). Fully coupled atmospheric-hydrological modeling at regional and long-term scales: Development, application, and analysis of WRF-HMS. *Water Resources Research*, *52*, 3187–3211. https://doi.org/10.1002/2015WR018185

Wei, J., Knoche, H. R., & Kunstmann, H. (2015). Contribution of transpiration and evaporation to precipitation: An ET-Tagging study for the Poyang Lake region in Southeast China. *Journal of Geophysical Research: Atmosphere*, *120*, 6845–6864. https://doi.org/10.1002/2014jd022975

Weldeab, S., Stuut, J.-B. W., Schneider, R. R., & Siebel, W. (2013). Holocene climate variability in the winter rainfall zone of South Africa. *Climate of the Past*, *9*, 2347–2364. https://doi.org/10.5194/cp-9-2347-2013

Werner, M., Haese, B., Xu, X., Zhang, X., Butzin, M., & Lohmann, G. (2016). Glacial–interglacial changes in H218O, HDO and deuterium excess—Results from the fully coupled ECHAM5/MPI-OM Earth system model. *Geoscientific Model Development*, *9*, 647–670. https://doi.org/10.5194/gmd-9-647-2016

Wong, T. E., Nusbaumer, J., & Noone, D. C. (2017). Evaluation of modeled land-atmosphere exchanges with a comprehensive water isotope fractionation scheme in version 4 of the Community Land Model. *Journal of Advances in Modeling Earth Systems*, *9*, 978–1001. https://doi.org/10.1002/2016MS000842

Zhang, Z., Arnault, J., Wagner, S., Laux, P., & Kunstmann, H. (2019). Impact of lateral terrestrial water flow on land-atmosphere interactions in the Heihe River Basin in China: Fully coupled modeling and precipitation recycling analysis. *Journal of Geophysical Research: Atmospheres*, *124*, 8401–8423. https://doi.org/10.1029/2018JD030174

Zink, M., Kumar, R., Cuntz, M., & Samaniego, L. (2017). A high-resolution dataset of water fluxes and states for Germany accounting for parametric uncertainty. *Hydrology and Earth System Sciences*, *21*, 1769–1790. https://doi.org/10.5194/hess-21-1769-2017